الجمهورية الجزائرية الديمقراطية الشعبية
PEOPLE'S DEMOCRATIC REPUBLIC OF ALGERIA

وزارة التعليم العالي والبحث العلمي
MINISTRY OF HIGHER EDUCATION
AND SCIENTIFIC RESEARCH

جامعة باتنة

UNIVERSITY OF BATNA

كلية العلوم

FACULTY OF SCIENCES

معهد الفيزياء

PHYSICS DEPARTMENT

....

A Thesis

Presented By: **AYACHE Rachid**

Submitted to Physics Department in Partial Fulfillment of the Requirement for the Degree of Doctor in Applied Physics

Preparation and characterization of transition metal silicides (β-$FeSi_2$)

Jury Members:

President :	M. CHAHDI	Prof.	*University of Batna*
Supervisor :	A. BOUABELLOU	Prof.	*University of Constantine*
Examiners :			
	R. HALIMI	Prof.	*University of Constantine*
	A. BOUCENNA	Prof.	*University of Setif*
	A. BELGACEM-BOUZIDA	Prof.	*University of Batna*
	A. BOUDRIOUA	MC (HDR)	*University of Metz (France)*

Copyright © 2005 by AYACHE Rachid
All rights reserved

Acknowledgements

I would like to especially thank my supervisor Prof. A. BOUABELLOU, who gave me the possibility of working within his dynamic and productive research group. In the long and deep scientific discussions I had with him, I greatly appreciated his enormous physical sense and his profound passion for scientific research. He always stimulated me and gave me the best advices.

I thank heartily Mr. M. CHAHDI, Professor in the department of physics, university of Batna that accepted to preside the jury.

I thank Gentlemen R. HALIMI, Professor in the department of physics, university of Constantine, A. BOUCENNA, Professor in the department of physics, university of Setif, A. BELGACEM BOUZIDA, Professor in the department of physics, university of Batna and A. BOUDRIOUA HDR in the university of Metz (France) that honored me by their acceptation to exanimate my thesis.

Many thanks to Dr. E. RICHTER and Prof. W. MÖLLER who are introduced me to their laboratories in the Ion Beam Institute, at the Forschungszentrum Rossendorf (Dresden-Germany) where much of the experimental work presented here was performed. I'll not mention all the names of the people who certainly feel our deepest gratitude. A special thank goes to Dr. F. EICHHORN for his help with the X-Ray pole figure measurement, Dr. R. GRÖTZCHEL for the RBS analyses and Dr. A. MÜCKLICH for the TEM pictures.

Special thanks are due to Mr. A. DAAMOUCHE for his proof reading of the manuscript.

Contents

0.1 Introduction . . . 1

1 Silicides and thin film formation **2**
1.1 Introduction . . . 2
1.2 Fe-Si system . . . 3
1.3 Epitaxial silicide formation . . . 5
1.3.1 Deposition techniques . . . 5
1.3.2 Ion beam techniques . . . 8
1.3.3 Ion beam mixing . . . 8
1.3.4 Ion beam synthesis . . . 8
1.3.5 Implanting at high doses . . . 10
1.3.6 Ion Implantation Technology . . . 15
1.4 Computer Simulation . . . 18
1.4.1 TRIM . . . 18

2 Microstructure of $\beta - FeSi_2$ **21**
2.1 Rutherford backscattering spectrometry (RBS) . . . 22
2.1.1 RBS concept . . . 22
2.2 RBS Theory . . . 23
2.2.1 Kinematic factor and electron energy loss . . . 23
2.2.2 Backscattering yield - Scattering cross section . . . 25
2.3 X-ray diffraction . . . 26
2.4 Bragg's law . . . 26
2.5 Transmission electron microscopy (TEM) . . . 29
2.5.1 Diffraction contrast . . . 29
2.5.2 Phase contrast . . . 30
2.6 TEM specimen preparation by ion-milling . . . 31
2.7 TEM specimen preparation by cleavage . . . 33
2.8 Electron diffraction . . . 34
2.9 Experimental details . . . 37
2.10 Results and discussion . . . 37
2.11 Conclusion . . . 42

3 Optical characterization 44
3.1 The Raman Effect . . . 44
3.2 Polarizability . . . 45
3.3 Infrared (IR) transmission and absorption spectroscopies . . . 49
3.4 Fourier Transform Infra Red . . . 49
3.5 Experimental . . . 52
3.6 Results and discussion . . . 53
3.7 Conclusion . . . 56

4 Structural and optical properties of $\beta - FeSi_2$ phase prepared by IBS 57

I Influence of implantation temperature 58
4.1 Experimental details . . . 59
4.1.1 Results and discussion . . . 59
4.1.2 Conclusion . . . 62

II Influence of dose 67
4.2 Experimental procedure . . . 68
4.2.1 Results and discussion . . . 68
4.2.2 Conclusion . . . 74

List of Figures

1.1 Bulk phase diagram of iron-silicon compounds (atfter Hansen-Ref. 17) 4
1.2 Bulk unit cells of the proposed film stabilized crystal structures: *(a)* $c-FeSi$ (eight $CsCl$ type unit cell), *(b)* $\gamma-FeSi_2$ (CaF_2 type), and *(c)* $\alpha-FeSi_2$. Side view of (111)−oriented film of $c-FeSi$ *(d)*, and *(e)* $\gamma-FeSi_2$ repectively *(f)* (112)-oriented film of $\alpha-FeSi_2$ . . . 4
1.3 C-centered Orthorhombic (Dusausoy et al., Acta Cryst. B27, 1209) 5
1.4 The unit cells the crystalline and reciprocal lattices of $\beta-FeSi_2$ are end-centered orthorhombic,with the extra lattice points centered on the c face by convention. The lengths of the reciprocal lattice vectors were calculated assuming $b \approx c = 7.8$ Å and $a \approx 9.9$ Å. The conventional crystalline unit cell on which the Miller indices are based is that of a simple orthorhombic lattice having the same parameters. 6
1.5 Epitaxial silicide forming techniques: (a) deposition techniques, (b) ion beam mixing and (c) ion beam synthesis [14]. 7
1.6 Nuclear and electronic energy loss [38] 10
1.7 The Ion Implanter 16
1.8 Ion and recoil trajectories for ten Fe^+ pseudoparticles entered the target under incidence of 7° with $195KeV$. Note that, along the projectile trajectories subcascades emerge which are caused by recoil atoms. 19
1.9 The implantation profile. 20

2.1 (a) macroscopic view and (b) atomic view on elastic collision between projectile ion and target atom. 22
2.2 Random RBS data for 150 nm of Fe deposited onto $Si(111)$ 23
2.3 Energy loss during RBS. The projectile loses energy on the inward path ΔE_{in}, during the collision ΔE_S and on the outward path ΔE_{out} [44]. . 25
2.4 Diffraction of coherent beam on a set of planes 27
2.5 Outline of (a) the goniometer axes and (b) the coordinate system. . . . 28
2.6 Ray diagrams showing the principles of formation of (a) BF contrast and (b) DF contrast. The dashed rays will not contribute to the final image. 30
2.7 Scheme of cross-section TEM sample preparation: (a) two stripes of material containing areas of interest are glued face-to-face,(b) the sample is dimpled on the upper side and ion-milled from both sides. 32

2.8 Cleavage plane orientations for $[111]Si$ wafer; a_1, a_2 and a_3 are the vectors of the unit cell. 34
2.9 (a) RBS spectrum of $195keV$ Fe ion implanted $(111)Si$ substrate at $500°C$ with a dose of $2x10^{17}Fe^+/cm^2$. $(b)Fe$ depth profile deduced from (a). 38
2.10 RBS Random spectra of 195 KeV Fe^+ implanted into $(111)Si$ substrate with a dose of $2x10^{17}$ Fe^+/cm^2 for as-implanted and subsequently annealed samples in a N_2 atmosphere during $90min$ at $850°C$ and $1000°C$. 39
2.11 (a) X-ray pole figure plot of (220) diffraction peak of $\beta - FeSi_2$ and (111) Si for the sample implanted and annealed at $850°C$ for $90min$. (b) XRD Spectrum scanning at the pole position of point 'z' in figure 2.9(a). (c) Partial pole figure of the $(101)\alpha - FeSi_2$ reflections at the scattering angle 2 θ=37.668° 41
2.12 Cross-sectional TEM images of 195 KeV Fe^+ implanted $(111)Si$ substrate at $500°C$ with a dose of $2x10^{17}$ Fe^+/cm^2 : (a) as-implanted, (b) annealed in a N_2 atmosphere at $850°C$ for $90min$. 43

3.1 Schematic illustration of Raman and Rayleigh scattering and infrared absorption 46
3.2 Schematic representation of a Raman spectrometer. 48
3.3 IR Spectra of samples before (as-implanted at $T_i = 500°C$) and annealing in N_2 atmosphere for $90min$ at $850°C$ 54
3.4 Raman scattering spectra at RT for the as-implanted and annealed samples. 55
3.5 Photoluminescence spectrum of $\beta - FeSi_2$ precipitate layer at $T = 12$ K for the sample annealed in a N_2 atmosphere during $90min$ at $850°C$. 56

4.1 (a) RBS spectrum for the as-implanted samples, (b) Fe and Si depth profiles deduced from (a). 60
4.2 RBS spectra for the as-implanted and annealed samples. 61
4.3 XRD pole figures for the as-implanted (a) and annealed (b) samples. . 63
4.4 Raman scattering spectra at RT for the as-implanted and annealed samples. 64
4.5 PL spectrum measured at $12K$ of $\beta - FeSi_2$ layer for the annealed sample. 65
4.6 (a) Random RBS data for the as-implanted samples at RT. (b) Fe and Si depth profile deduced from the RUMP analysis. 69
4.7 RBS spectra for the as-implanted and annealed samples at $850°C$ for different times. 70
4.8 XRD patterns of the as-implanted and annealed samples for different annealing time at $850°C$. 71
4.9 Cross-sectional TEM images of 195 keV Fe^+ implanted $(111)Si$ substrate at RT with a dose of $8x10^{17}Fe^+/cm^2$: (a) as-implanted, (b) annealed in a N_2 atmosphere at $850°C$ for $4h$. The inset (Fig. 4.9a) shows the corresponding electron diffraction pattern of the $\beta - FeSi_2$. 72
4.10 IR spectra for the as-implanted and annealed samples.Inset shows the latter transmittance for the as-implanted sample. 73

4.11 Raman scattering spectrum at RT for the as-implanted and annealed samples. 74

0.1 Introduction

Iron ion implantation into silicon is a suitable way for the formation of buried semiconducting iron disilicide ($\beta - FeSi_2$) layers which have interesting and promising properties and offer various applications. The $\beta - FeSi_2$ phase is orthorhombic with lattice constants $a = 0.9865nm$, $b = 0.7791nm$, and $c = 0.7833nm$ at room temperature [1]. The $\beta - FeSi_2$ is a novel direct band gap semiconductors with $Eg = 0.85 - 0.87eV$, which matches the wavelength of 1.5 μm of silica optical fibers [2, 3 , 4, 5]. Thus, making it suitable for optoelectronic communications. Therefore, $\beta - FeSi_2$ phase is potentially of interest for use in future solar cells, infrared detectors and light emitters as well as thermoelectronics devices [6]. The $\beta - FeSi_2$ is also known to be a Kankyo semiconductor (ecological friendly semiconductor)[7].

Several techniques have been used for the preparation of $\beta - FeSi_2$, such as reactive deposition epitaxy [8], pulsed laser deposition (PLD) [9], ion beam assisted deposition (IBAD)[10, 11] and ion beam mixing (IBM) [12, 13]. Previous studies showed that the most $\beta - FeSi_2$ with the best results was fabricated by ion beam synthesis (IBS) [4, 14, 15, 16]. Conventional IBS technique consists of two steps. First, incident ions with very high energy and dose are implanted into silicon substrates, and second, after implantation, annealing is conducted to remove the residual damage induced by the implantation process and to redistribute the implanted ions into a well-defined layer.

The aim of this thesis is to study in details the structural and optical properties of iron silicide formed by ion beam synthesis. This thesis is organized as follows:

Chapter 1 introcduces the most important properties of silicides and thin film formation. The basic concepts concerning epitaxial layers on a substrate and ion beam synthesis (IBS) are explained.

In Chapter 2: (Part I) The concepts of a wide variety of analysis techniques such as Rutherford backscattering spectrometry (RBS), X-ray diffraction (XRD) and transmission electron microscopy (TEM) are explained. In Part II, these techniques have been applied to investigate the structural properties of the synthesized materials.

Chapter 3 focuses on general concepts of optical analyzing techniques. In this chapter, we report the vibrational properties and PL emissions of the $\beta - FeSi_2$ investigated by infrared (IR), Raman spectroscopies and photoluminescence (PL).

In Chapter 4 we study the structural and optical properties of $\beta - FeSi_2$ phase prepared by IBS at different implantation temperature of substrate and different dose. Finaly, the Thesis is summarized.

Chapter 1

Silicides and thin film formation

1.1 Introduction

The applications of Si-based binary systems in the microelectronics industry [17] have stimulated silicide research over the last years. The ever increasing demand of a larger integration requires the manufacture of smaller and smaller devices. This can be accomplished only by developing new materials able to bridge the relevant technological problems. Thus, the needs to scale down transistors prompted the use of silicides to decrease junction resistivities. In this context, silicides are being successfully used in the latest generation of chips because they exhibit several unsurpassed properties when compared to other materials, for instance their ability to form stable contacts with Si. On the other hand, Si-based binary systems have received a lot of attention in Surface Science because of their interesting fundamental physics. Both reactive and non-reactive interfaces can be obtained when a second element is implanted or deposited onto a Si substrate [18].

In the case of a metal, the formation of a Schottky barrier takes place [19]. Most metal/silicon interfaces are reactive and in this case a silicide layer is formed after metal deposition. Silicides can be classified in three large groups. In the first group we find refractory-metal silicides, used because of their high thermal stability (e.g. WSi_2 and $TiSi_2$). The second group are near-noble metal silicides, characterized by a low chemical reactivity, as $PtSi$ and $CoSi_2$[20]. Finally, rare-earth metal silicides (like $ErSi_2$) are able to absorb infrared light and thus are investigated as potential constituents of infrared detectors. If we restrict ourselves to transition metal silicides, excellent perspectives exist for future use of $CoSi_2$. This compound has been implemented down to $0.1pm$ technology without problems. Other interesting features are its excellent epitaxial growth on Si [21], which favor more stable contacts. Other good

candidates are $NiSi_2$ [22]and $FeSi_2$.

1.2 Fe-Si system

The reacted silicides often assume crystal structures that are stabilized in thin-film geometry only and are not present in the silicon–metal bulk phase diagram. In the case of iron, to which we focus in the present work, the bulk phase diagram contains three stable crystal structures for certain atomic compositions at room temperature [23] as displayed in figure 1.1. We concentrate in particular on the example of 50% atomic Si content, where semimetallic $\varepsilon - FeSi$ crystallizes in the $B20$ structure, [24, 25] and of 67% atomic Si content, where the semiconducting $\beta - FeSi_2$ phase develops in orthorhombic crystal structure [25]. At this composition, an additional metallic phase, $\alpha - FeSi_2$ is stable at elevated temperatures of above $950°C$ [25]. Ultra thin films, however, assume different crystal structures as reported by several groups [26, 21]. At 1:1 stoichiometry, instead of $\varepsilon - FeSi$ a phase of $CsCl$ crystal structure ($c - FeSi$) has been reported [21, 27, 28, 29]. The phase at 67% silicon exhibits also a symmetry different from the bulk with, however, the structure still under debate. The CaF_2 structure ($\gamma - FeSi_2$), an iron depleted defect $CsCl$ structure and an $\alpha - FeSi_2$ derived structure have been proposed [30, 31, 32, 33]. The crystal structures of these phases are displayed in figure 1.2. panels (a) and (b) show the cubic CsCl (eight unit cells for comparison) and CaF_2 structures, respectively. Indicated by the gray shading, {111}-oriented planes are included. The tetragonal unit cell of $\alpha - FeSi_2$ is plotted in panel (c) which with unit vectors of $a = b = 2.68$ Å and $c = 5.14$ Å roughly compares to the volume of two $CsCl$ cubes. Side view projections in $[\bar{1}\bar{1}0]$direction of the respective films fitting on Si(111) are displayed in panels (d–f). For CsCl (panel d) and CaF_2 (panel e) these films are oriented in [111] direction. For the $\alpha - FeSi_2$ film,the corresponding surface orientation is (112), i.e., normal to the [221] direction, and would imply expansion in [001]direction for an isotropic lattice match on $Si(111)$. Bonds within the projection plane are indicated by single lines. Double lines indicate bonds to two atoms, one in front of and one behind the projection plane. The growth conditions prove to be of important influence for the development of the different crystal structures. The most widely accepted source of information on the crystal structure of $\beta - FeSi_2$ is the article by Dusausoy et al. [34].

The unit cell of the end-centered crystalline lattice is shown in figure 1.3. Figure 1.3 and figure 1.4 present the unit cells of the crystalline and reciprocal lattices of $\beta - FeSi_2$ are end-centered orthorhombic, with the extra lattice points centered on the c face by convention. The lengths of the reciprocal lattice vectors were calculated assuming $b \approx c = 7.8Å$ and $a \approx 9.9Å$.The conventional crystalline unit cell on which

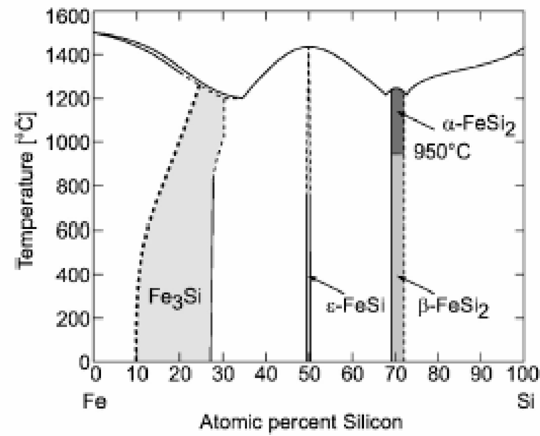

Figure 1.1: Bulk phase diagram of iron-silicon compounds (atfter Hansen-Ref. 17)

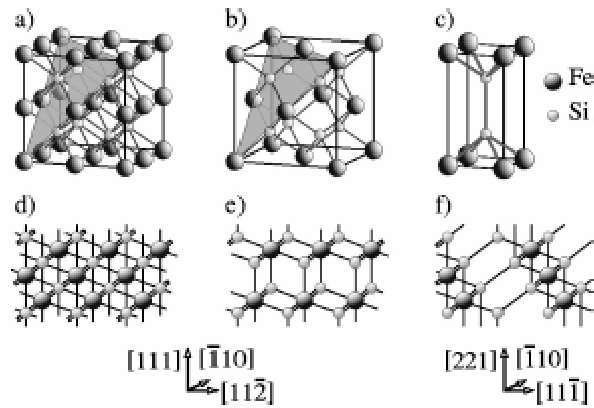

Figure 1.2: Bulk unit cells of the proposed film stabilized crystal structures: *(a)* $c-FeSi$ (eight $CsCl$ type unit cell), *(b)* $\gamma-FeSi_2$ (CaF_2 type), and *(c)* $\alpha-FeSi_2$. Side view of (111)−oriented film of $c-FeSi$ *(d),* and *(e)* $\gamma-FeSi_2$ repectively *(f)* (112)-oriented film of $\alpha-FeSi_2$

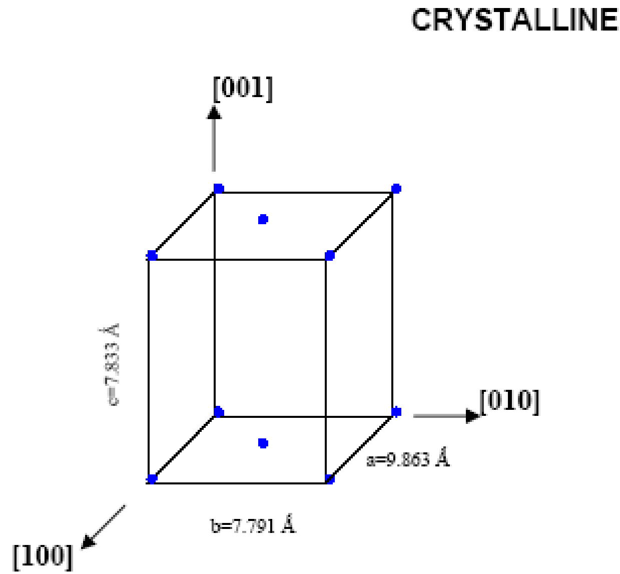

Figure 1.3: C-centered Orthorhombic (Dusausoy et al., Acta Cryst. B27, 1209)

the Miller indices are based is that of a simple orthorhombic lattice having the same parameters.

Although the slight difference between b and c is crucial for heteroepitaxial matching, it is not so for the basic structure lattice of the transmission diffraction pattern. For growth on $Si(111)$, the observed heteroepitaxial relationships are [35, 36] $FeSi_2(110)/Si(111)$ with $FeSi_2[001]||Si < 011 >$ and $FeSi_2(101)/Si(111)$ with $FeSi_2[010]||Si < 011 >$

1.3 Epitaxial silicide formation

Epitaxial silicides can be formed using a number of variations on two basic methods. In general we can classify these procedures as either deposition techniques or ion beam techniques.

1.3.1 Deposition techniques

Deposition techniques (figure 1.5(a)) involve evaporation of metal layers onto the silicon substrate under vacuum conditions. The sample is then annealed in order to initiate the silicide forming reaction which usually takes place significantly below the melting point of the materials. Accordingly this method of compound formation is termed solid phase epitaxy (SPE). Thermal evaporation of the metal is usually achieved using

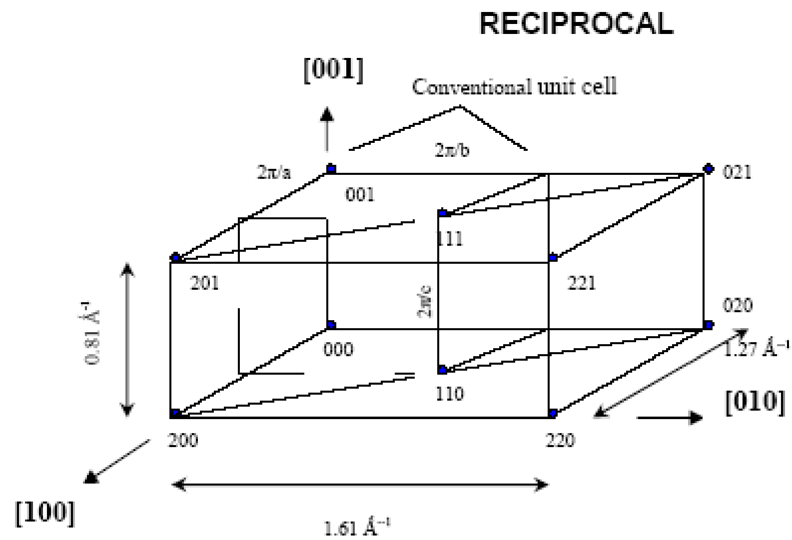

Figure 1.4: The unit cells the crystalline and reciprocal lattices of $\beta - FeSi_2$ are end-centered orthorhombic,with the extra lattice points centered on the c face by convention. The lengths of the reciprocal lattice vectors were calculated assuming $b \approx c = 7.8$ Å and $a \approx 9.9$ Å. The conventional crystalline unit cell on which the Miller indices are based is that of a simple orthorhombic lattice having the same parameters.

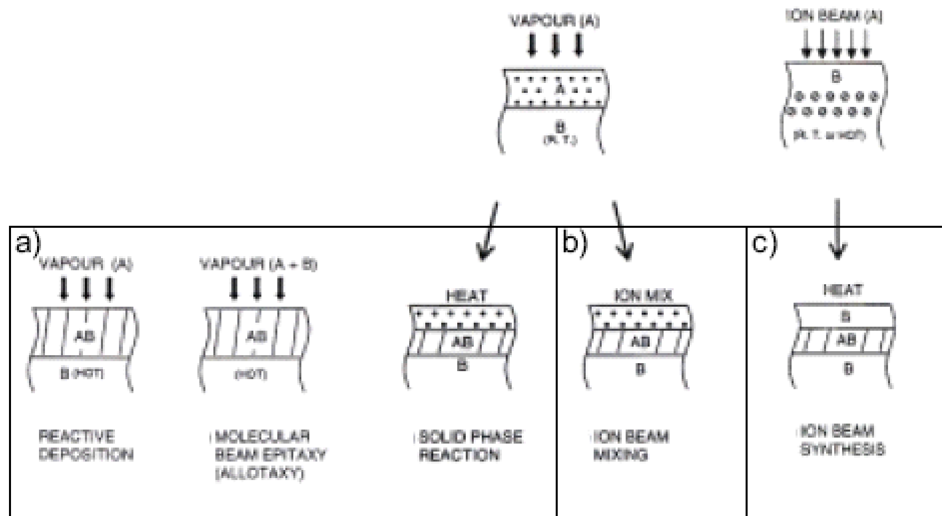

Figure 1.5: Epitaxial silicide forming techniques: (a) deposition techniques, (b) ion beam mixing and (c) ion beam synthesis [14].

resistive, inductive or laser heating or electron bombardment of the required metal to form a vapour. This vapour condenses when it comes into contact with the substrate, which is maintained at a lower temperature, forming a layer of metal on the silicon. Other methods of producing the initial film are sputtering and chemical vapour deposition (CVD). Sputtering involves the metal source being bombarded by energetic ions (usually of a noble gas) and releasing metal ions from the source, which form the film. In CVD, gases are decomposed by a chemical reaction to form the vapour. Considerable improvements in the achievable quality of evaporated films have been obtained since the introduction of molecular beam epitaxy (MBE). This occurs under ultra-high vacuum (UHV) conditions. It allows co-deposition of a stoichiometrically correct ratio of both the metal and silicon.

Thermal annealing of silicides is typically carried out at temperatures of the order of $1000°C$ for $\frac{1}{2}-1$ hour. Rapid thermal annealing (RTA) involves higher temperatures than conventional furnace annealing for a much shorter time span (typically for less than a minute). Laser annealing, using pulses of a laser radiation incident on the sample, can also be used. In all cases the purity of silicides formed by deposition depends on the cleanliness of the metals used for evaporation, the surface condition of the substrate and the annealing ambient. This has important consequences for the resistivity, crystalline quality and the epitaxy of the silicide.

1.3.2 Ion beam techniques

Beams of accelerated charged particles can be used either to induce the silicide forming reaction or to supply the material needed to form the silicide.

1.3.3 Ion beam mixing

Ion beams can be used as an alternative to thermal annealing to promote compound formation as indicated in figure 1.5(b). The evaporated layer is produced by one of the above mentioned methods. It is then bombarded by an ion beam of an inert gas or one of the silicide components. This can induce an intermixing between the film and the substrate and provides the necessary energy for the formation of the silicide.

1.3.4 Ion beam synthesis

Description

Ion implantation is the introduction of impurities into the surface layer of a solid substrate by bombardment of the target with high energy ($keV - MeV$) ions (figure1.5(c)). This process can alter almost all the physical properties of a solid. It is useful for a wide variety of applications. Low doses of radioactive probes can be implanted into samples for analysis purposes, doses around $10^{13} at/cm^2$can be used for the introduction of dopants into semiconductors, still higher levels of implantation can be used to produce supersaturated solutions of impurity materials in a target and very high doses can be used to actually alter the stoichiometry of a target by ion beam synthesis. The ions are produced in an ion source by sputtering a solid target or ionising a vapour, for example. They are extracted from the source and electrostatically accelerated. The desired isotope is then isolated using mass separation. For a given implantation energy, a magnet can be used to select an isotope according to its mass m per unit charge q. The radius R of the circular path of a charged particle in a magnetic field B is given by

$$R = \frac{1}{B} \frac{m}{q} \nu \tag{1.1}$$

where v is the ion velocity. Following the mass separation the ions are focused into a convergent beam which is then electrostatically scanned over the sample to produce a homogeneous implanted area.

Stopping and damage creation issues

When the ion enters the target, it undergoes a series of collisions with target electrons and nuclei, which causes its kinetic energy to be transferred to the substrate. Eventually the ion comes to rest within the target. The penetration depth of the ion depends upon a number of factors including the energy of the implanted ion, its mass and the mass of the substrate atoms. The slowing down process in ion implantation is governed by two mechanisms, electronic and nuclear stopping. This stopping is characterized by the stopping power dE/dx, the energy loss per unit depth. The total energy loss is taken to be the sum of the two components, $\left[\frac{dE}{dx}\right]_e$ and $\left[\frac{dE}{dx}\right]_n$for electronic and nuclear stopping respectively

$$\left[\frac{dE}{dx}\right] = \left[\frac{dE}{dx}\right]_e + \left[\frac{dE}{dx}\right]_n \tag{1.2}$$

Detailed discussions of stopping can be found in references [44, 38, 39].

Electronic Stopping

Electronic stopping occurs when the implanted ion either excites or ionizes target electrons. The momentum transfer is small due to the low mass of electrons so these can be generally approximated as inelastic collisions. The energy loss process consists of many collisions with electrons but due to the large number of electrons this can be actually considered as a continuous e,..ect. Only small detections of implanted ions take place due to electronic stopping. There are two regimes for electronic stopping. In the high energy regime (such as the one used for Rutherford backscattering (RBS)) the ion can be considered to be fully stripped of its electrons as it is traveling faster than their orbital velocity. Here, the stopping decreases with increasing velocity. At lower energies (such as those applicable for ion implantation) the stopping power increases with velocity as shown in figure 1.6. The boundary between these two regimes lies around $\ddot{v} \succ v_1 = Z_1^{\frac{2}{3}} v_0$, where v_0 is the velocity in the first Bohr orbit: $v_0 = \frac{e^2}{\hbar} =$ 2.1877x10$^6 m/s$.

Nuclear Stopping

At lower energies, particularly for high mass ions, nuclear stopping also plays an important role. If the implanted ion collides with target nuclei they will undergo an almost elastic collision. This can be essentially treated as a two body screened

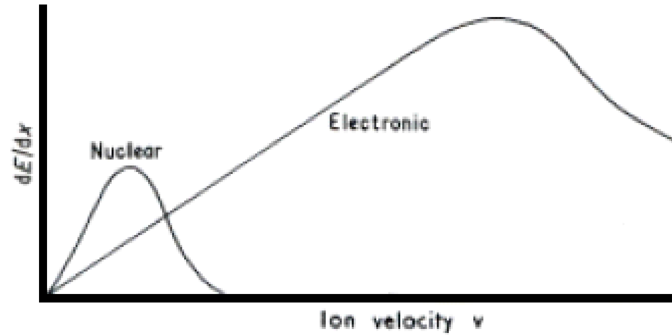

Figure 1.6: Nuclear and electronic energy loss [38]

Coulomb interaction. The projectile can experience large angular detections and lose a significant portion of its energy in a single collision. Such interactions need to be treated as discrete events. The lost energy is transferred to the target atom which can be displaced from its lattice site causing damage to the target in the form of lattice disorder. The velocity dependence of the nuclear energy loss is shown in figure 1.6.

Implantation profile

The path of a single projectile as well as its projected range, R_p, is random due to the stochastic nature of the stopping process within the collision cascade, the duration of which is approximately $10^{-13}s$. The spacial distribution of the implanted species is usually Gaussian-like with respect to the direction x perpendicular to the sample surface (longitudinal straggling)

$$N(x) = \frac{\phi}{\sqrt{2\pi}\Delta R_p} e^{-\frac{1}{2}\left(\frac{x-R_p}{\Delta R_p}\right)^2} \tag{1.3}$$

Where $\triangle R_p$ denotes the projected range straggling.

1.3.5 Implanting at high doses

Since there is no convenient absolute method of defining the high-dose domain, an arbitrary definition is usually employed. The implants with doses greater than $1 \times 10^{15} ions/cm^2$ are considered to be high-dose implants [40]. High-dose implantation is obviously associated with a large amount of radiation damage and high dopant concentration. Both damage and dopant concentration depend upon the energy of the implant, and the damage also depends upon a number of other implant parameters,

such as the mass of the implant species, the mass of the substrate, the dose rate, the scanning strategy used and the implantation temperature.

There are two general categories of problems associated with high-dose implants:

1- Those resulting from damage to the target; and

2- Those resulting from changes in target temperature.

The damage and its resultant effects arise from the dissipation of the kinetic energy of the ions into displacement and excitation of atoms in the target (wafer). During implantation the temperature rise can produce variations in the damage generated by the implant, both across the wafer (depending on the scanning technique), and between wafers (depending on the exact implantation conditions).

Ion beam heating

The energy of the ion beam is dissipated and ultimately converted into heat. This causes the temperature of the target to rise. If the target has a high thermal capacitance, the increase in the temperature will be negligible. However, semi-conductor wafers have a small thermal capacity; this significant temperature rises can occur.

A convenient parameter to use when considering beam heating is irradiance.

$$Irradiance = \frac{IE}{A} \quad (in\ W.m^{-2}) \tag{1.4}$$

Where I is the ion beam current in Amperes,

E is the ion energy in electron volts, and

A is the area (in m^2) scanned by the beam.

Damage generated in high-dose implants

The electrical behavior of high-dose implants is basically determined by the residual damage after annealing. Furthermore, the damage after annealing is a function of both the annealing process and a damage generated during implantation[41].

Implanted ions create zones of gross disorder in the region where the ion deposits its kinetic energy. The zones are vacancy rich in the centre and are surrounded by interstitial atoms. During high-dose implants, these zones may overlap and create a continuous amorphous layer. The energy deposition is approximately Gaussian in its depth distribution, so that the disorder is non-uniform in depth.

Range of Damage

The range of damage, or the region in which the lattice atoms are mostly displaced to, is of concern. This region also sees the formation of an amorphous layer, which

may or may not be desired. It is instructive to realize that the energy transfer of the impending ions is non-linear. The point, at which maximum energy is transferred, is not at the end of the motion. Therefore, the implanted ion range is not equal to the damage range. In fact, the damage range occurs near the surface of the target.

(1) Implanted range of the ions > Range of the damage.

(2) The implanted ion range approaches the damage range as the ions get heavier.

(3) Standard deviation of the ion range < Standard deviation of the damage range. (Light ions)

(4) Standard deviation of the ion range > Standard deviation of the damage range. (Heavy ions)

As the implanting energies increases, the damage range draws away from the surface and gets deeper until it approaches the implanted range.

Amorphous Layer

Formation of an amorphous layer as a result of ion displacement is unavoidable during the implant process. This can serve or disrupt the process depending on the fabrication process. However, the amorphous layer is formed only during a critical implanting dose. The critical implanting dose is given by: (a simple formula)

$$N_{(implanted\ dose)a} = 2E_d N/(dE/dx)_n \tag{1.5}$$

where $N = number\ of\ ions$

(an advanced formula)

$$N'_{(implanted\ dose)a} = \left(N_{(implanted\ dose)a}/2)\right) \left[1 - \left(\delta R N_{(implanted\ dose)a}\right)/2\right]^{-2} \tag{1.6}$$

where $\delta R = 2\sqrt{D_v t}$ and $D_v = Diffusivity$

The advanced formula considers the following extra points:-

(1) Diffusion

(2) Secondary collisions

(3) Temperature effects

Note : A higher critical dose is necessary for higher temperatures. On the other hand, a lower critical dose is required as the dose rate increases.

Radiation Damage

Radiation damage arise under nuclear interactions between the implanting ions and the target atoms. The physics behind this is covered within the sub-page of 'Nuclear

Interactions'. Radiation damage cannot be avoided and will always be present in which two types are significant:

(1) Simple displacements of atoms known as Frenkel Defects.

(2) Cluster type complex defects.

As the implanting ions pass through the target substrate, they undergo collisions with the lattice, displacing the target atoms before they themselves come to rest. Several factors are worth considering during this occurrence:-

(1) The number of lattice atoms displaced, N_d.

(2) Range of this damage, R_D (not equal to R_p).

(3) Formation of an amorphous region as a result of these atomic displacements.

Number of atoms displaced

In the calculation of this value, the energy imparted from the ions is used. Alternately, the number of vacancies arising can be used in the computation.

$$N_D = \frac{E}{2E_d} \tag{1.7}$$

where E_d is displacement energy and E is ion energy.

This equation is valid for ranges below a critical value (For Si, this value is $36.3keV$)

Note 1: *At higher energies, this calculated number of displaced atoms actually decreases. This is involves electronic stopping. Initially, only nuclear stopping decreases the ion energy at low energy ranges.*

Channeling effect

Crystalline structures implies lattice planes which act like channels in which an implanted ion can travel without nuclear interactions such as collisions. This effect is constantly avoided and purposeful usage of this phenomenon is not widely advised. However, it is dependent on some factors which serve to eradicate its 'ill-effects'. Channeling depends primarily upon:

(1) The critical angle of approach and therefore the orientation of the target

(2) Temperature effects

(3) Amorphization

Critical Angle

The critical angle is the angle in which an ion can enter a channel without leaving it. As long as the vertical component of the ion's energy is smaller than the repelling potential of the atomic chain, the ion remains within the channel. This vertical component of energy is orientation-dependent.

Two expressions are available for two energy ranges:-

$$Q_{c_1} = \sqrt{\frac{2Z_1Z_2q^2}{E_d}} \tag{1.8}$$

where $E \geqslant 2Z_1Z_2q^2/a^2$

$$Q_{c_2} = \left[\frac{Q_{c_1}\sqrt{3}a}{\sqrt{2}d}\right]^{\frac{1}{2}} \tag{1.9}$$

where $E \leqslant 2Z_1Z_2q^2/a^2$

(d is distance between atoms and a is lattice parameter)

This critical angle increases for ion mass increase and decreases for implantation energy increase.

Temperature Effects

As the temperature of the implant is increased, the lattice atoms acquire more energy. This results in some ions being scattered out of the channels. This scattering is increased with increasing temperatures.

Amorphization

Amorphization of the substrate or target through radiation damage or purposeful manipulations imply destruction of crystalline structures and consequent eradication of channels. This is the only method to totally prevent channeling effects.

A similar effect in use is the usage of a 'Scattering Layer' in which an amorphous coating is first applied to the target before the implant. This will prevent passage of the ions into the channels. However, this is not guaranteed.

Subsidiary Points

With purposeful orientations of the target, we can prevent channeling to a certain degree. The usual preventive orientation is 7 to 10 degrees from the normal.

Critical dose of implanting ions give rise to radiation induced amorphization, this amorphous layer eradicates the effect of channeling. If this amorphization is desired, an operating critical dose can always be maintained. ('Critical dose' is discussed under the sub-heading of Damage.)

However, it must be maintained that channeling effect is not severe. Under all circumstances, the maximum range of the implanted ions are never affected.

1.3.6 Ion Implantation Technology

A Typical Ion Implanter

The major components in an ion implanter are the ion source, the extracting mechanism, the ion analyzing system, the accelerating column, the scanning station, and the end station (see figure 1.7).

The Ion Source

The ion source is the most important component of the implanter. All sources produce ions by using a confined electrical discharge sustained by the gas or vapor of the material to be ionized. Most ion sources consist of positive ions, but in the case of high-energy implants, negative ion sources are needed.

The Ion Extracting Mechanism

The desired species to be implanted into the substrate must be present in the beam as charged particles, and thus the ionization process is important in determining the concentration of the beam current extracted from the source. Positive ions are most commonly created by inelastic collisions with high-energy electrons that supply enough energy to remove an electron from the atom or from the ion. In other words, the atom gains energy greater or equal to its ionization potential.

Once ionized, the ions and electrons form gas plasma with no space charge. Since the gas contains equal numbers of ions and electrons, it can be considered as field free. During extraction, the current between the cathode, anode and gas inlet should be adjusted to maintain stable gas discharge so that the positive ions can be extracted by electrode extraction.

The Ion Analyzing System

Since ions extracted from the source may contain many different ion species due to the different atomic and molecular species in the discharge chamber, magnetic mass analyzers are used to separate those desired ion species from the other different species, as well as remove residual air, hydrocarbons from vacuum pumps, and other impurities.

The ions enter a region with a magnetic field normal to their paths and are deflected according to the formula:

$$\overrightarrow{F} = q\overrightarrow{v} \wedge \overrightarrow{B} \tag{1.10}$$

where $\overrightarrow{B}$ is the magnetic flux density,

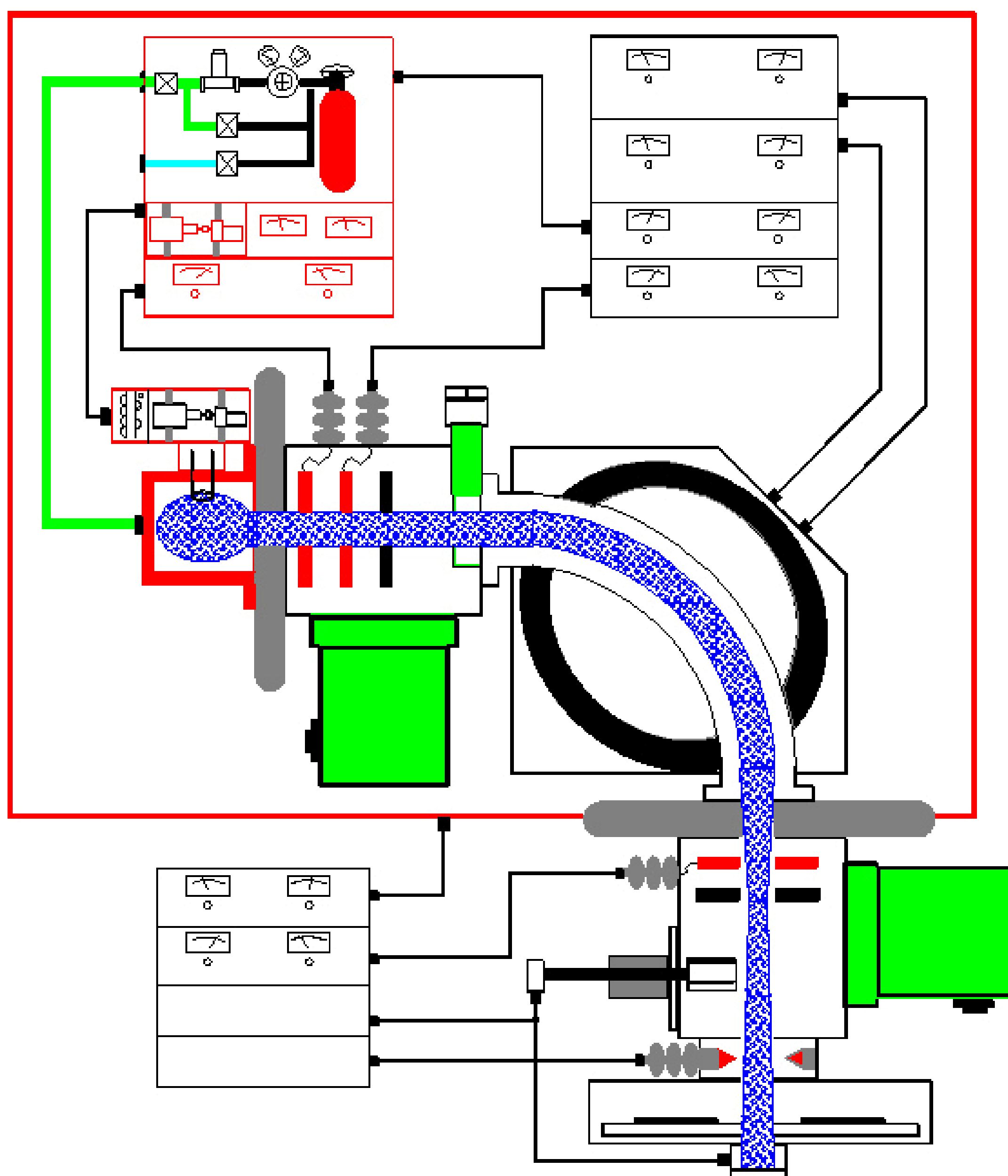

Figure 1.7: The Ion Implanter

$\overrightarrow{F}$ is the force on the ions,

q is the charge of the ions, and

$\overrightarrow{v}$ is the velocity of the ions

If the magnetic field is homogeneous, then the ions move in a circular path, of which the centrifugal force is given by:

$$F = (Mv^2)/r \tag{1.11}$$

Combining the two equations,

$$r = \frac{Mv}{qB} = \frac{\sqrt{2EM}}{qB} \tag{1.12}$$

Thus, for extraction voltage V, the kinetic energy, so that

$$r = \sqrt{\frac{2MV}{q}\frac{1}{B}} \tag{1.13}$$

The Accelerating Column

The accelerating column does not only accelerate the ions by passing them through potential differences to gain kinetic energy, but at the same time subjects the ions to magnetic and electric fields that focus the ion beams. This focusing is required since the beam of ions leaving the source is naturally divergent.

A typical accelerator tube is made up of a series of electrodes separated by insulators. The overall acceleration voltage is distributed over the electrodes. The extraction voltage is of the order $10 - 20kV$, while the acceleration voltage ranges between $60 - 200kV$ according to the implanter.

The Scanning Station

The main advantage of ion implantation is that the total dose and the dose rate may be electrically monitored. Scans are usually performed by electrostatic fields, a mechanical movement of the target or a combination of both.

The measurement of dose is made by placing a current integrator between the target and the ground and counting the total collected current from the incident ions. From the total dose value obtained, the dose rate may be calculated.

The End Station

At the end station, the beam of ions finally hits the target and implants the ions into the wafer. A diffusion pump located at the end station pumps out all residual air in the target chamber, leaving a vacuum for the ions to travel in.

1.4 Computer Simulation

1.4.1 TRIM

The widely used TRIM (transport of ions in matter) simulation program describes the path of an incident projectile as a series of binary collisions with target atoms at rest. Thermal vibrations of matrix atoms around their positions are neglected. The momentum transfer in a single projectile-target collision occurs within a time frame much shorter than a period of lattice vibration at RT (10^{-13}-10^{-12}s). Thus, the atoms of the matrix can legitimately be assumed to be motionless at RT.

The target atoms are quasi-randomly distributed in space which applies in a first approximation to amorphous materials, even though a short range order does always occur in reality.

The path of the ion is characterized by a constant free path length, λ,which the projectile travels between two seccessive collisions. Here, λ is given by the inverse cube root of the atomic density.

From a simulative point of view, the randomness is realized by a randomely generated impact parameter for each individual binary collision. From this, each nuclear collision is characterized, i.e. the nuclear energy loss as well as the polar deflection angle are calculated using the universal screening potential given by the following equations:

$$V(r) = \frac{Z_1 Z_2 e^2}{4\pi\epsilon_0 r}\chi\left(\frac{r}{a}\right) \tag{1.14}$$

where χ and a denote the screening function and the screening length, respectively. The other variables bear common meaning.

Numerous variations of χ were developed to describe the potentials of as many projectile-target combination as possible. Finally, a universal screening function

$$\chi_{uni}(y) = 0.1818e^{-3.2y} + 0.5099e^{-0.9423y} + 0.2802e^{-0.4028y} + 0.02817e^{-0.2016y} \tag{1.15}$$

was established by Zieglar [64], including a universal screening length

$$\frac{r}{y} = a_{uni} = \frac{0.8845a_0}{Z_1^{0.23} + Z_2^{0.23}} \tag{1.16}$$

where $a_0 = 0.053nm$ denotes the first Bohr radius of the hydrogen atom.

Besides that, the electronic energy loss of each particle in motion is recorded on the intercollisional paths.

Consequently, positional, directional, and energetic changes of the projectile describe its path through the matrix.

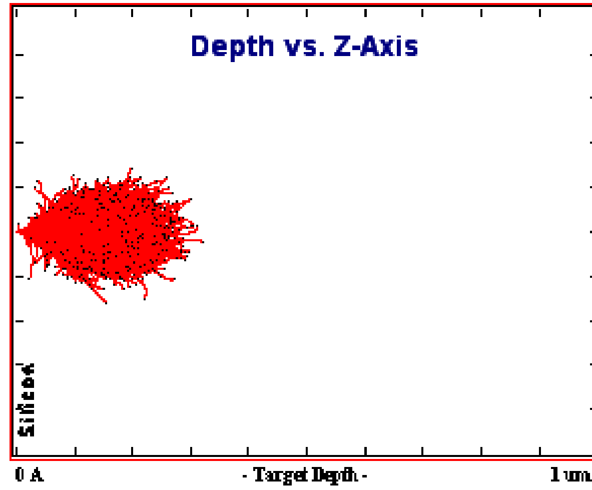

Figure 1.8: Ion and recoil trajectories for Fe^{+} pseudoparticles entered the target under incidence of 7° with $195 KeV$. Note that, along the projectile trajectories subcascades emerge which are caused by recoil atoms.

For illustration, figure 1.8 depicts the collision cascades of pseudoparticles for a target silicon. And also the implantation profile is presented in figure 1.9.

Prior to the simulation run, the target and projectile parameters (width of the layers, atomic densities, number of pseudoparticules, initial projectile energy, and angle of incidence) have to be declared in the table.

Furthermore, certain element specific energy parameters are predefined, namely E_d (the displacement energy above which a stable interstitial-Frenkel pair is formed), E_s (the surface binding energy), and E_b (the bulk binding energy which substracted from the nuclear energy transfer). The determination of E_b is not uniform throughout literature. Some authors set E_b equal to zero, although E_b is generally interpreted as vacancy formation energy, i.e. as the minimum energy of an atom to leave the lattice site.

Target Data

Fe (195Kev) into Si(111)

Layer Name	**Density**	**Fe (56)**	**Si(28)**	**Solid/Gas**
Iron	7.866	1	0	Solid
Silicon	2.321	0	1	Solid
Lattice Binding energy (eV)		3	2	
Surface Binding energy (eV)		4.34	4.7	
Displacement energy (eV)		25	16	

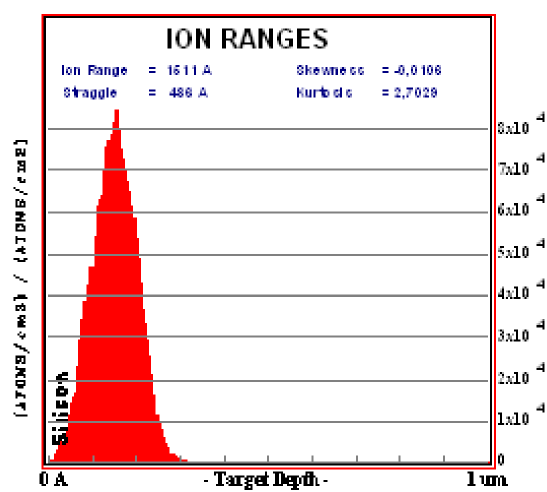

Figure 1.9: The implantation profile.

Chapter 2

Microstructure of $\beta - FeSi_2$

Part I: Analysis Techniques

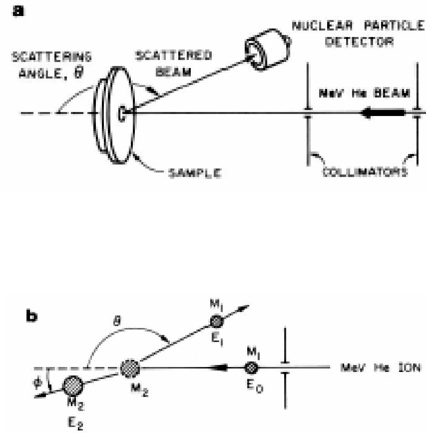

Figure 2.1: (a) macroscopic view and (b) atomic view on elastic collision between projectile ion and target atom.

2.1 Rutherford backscattering spectrometry (RBS)

Rutherford backscattering spectrometry combined with channeling is a powerful technique to determine composition, thickness and crystalline quality of thin films. RBS is based on the well known and pioneering experiments of Rutherford and his students Geiger and Marsden in 1911 in which they studied the scattering of highly energetic $\alpha-$particles on a thin gold film. Their experiments led to a new model for the structure of the atom. Up to now, a slightly adapted version of their model is still valid. The aim of this part is to explain how the physical properties such as thickness, composition and crystalline quality can be deduced from the experimental data. An elaborate description on RBS and channeling can be found in [42, 43].

2.1.1 RBS concept

As is shown in figure 2.1 (a), a well collimated high energy beam (in our case $1.7MeV$) of He^+ ions impinges on the target. The backscattered He projectiles are collected in a surface barrier detector generating an electric signal proportional to the energy of the detected projectile[44]. The detector is coupled to a amplifier and an multi channel analyzer (MCA). Depending on the energy of the backscattered particle, the count will be placed in a certain channel when passing the MCA. In this way, a backscattered yield as a function of energy spectrum or an RBS spectrum is built up.

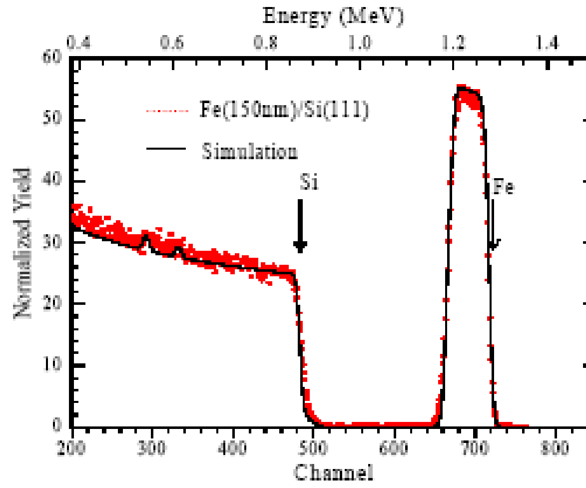

Figure 2.2: Random RBS data for 150 nm of Fe deposited onto $Si(111)$

2.2 RBS Theory

As described above, an RBS spectrum consists of a plot of the number of backscattered He projectiles as a function of their energy. A typical spectrum is shown in figure 2.2. In the following part, the different aspects determining the quantity and the energy of the backscattered particles will be elucidated. From the energy of the backscattered particle, the mass of the target atom and its depth can be deduced. The amount of particles detected with a certain energy can be correlated to the concentration of a specific target element.

2.2.1 Kinematic factor and electron energy loss

In this part, we will investigate the mechanisms which determine the energy of the backscattered He projectile. Hence, we will elucidate the different mechanisms which determine the mass and the depth of the target atom.

Figure 2.1 (b) describes the collision between an incident particle and a target atom[45]. The process can be described solely using principles of classical mechanics. Since, the collision is elastic, there is conservation of kinetic energy. This principle together with conservation of momentum, results in the following set of equations

$$\frac{1}{2}M_1 v^2 = \frac{1}{2}M_1 v_1^2 + \frac{1}{2}M_2 v_2^2 \tag{2.1}$$

$$M_1 v = M_1 v_1 \cos\theta + M_2 v_2 \cos\phi \tag{2.2}$$

$$0 = M_1 v_1 \sin\theta + M_2 v_2 \sin\phi \tag{2.3}$$

From this, the ratio between the projectile energies E_1 and E_0 can be calculated assuming that $M_1 < M_2$

$$K_{M_2} = \frac{E_1}{E_0} = \left[\frac{\left(M_2^2 - M_1^2 \sin^2\theta\right)^{\frac{1}{2}} + M_1 \cos\theta}{M_1 + M_2} \right]^2 \tag{2.4}$$

with E_0 the energy of the projectile before collision and E_1 the energy of the projectile after collision. The ratio of E_1 and E_0 is called the kinematic factor K. This formula reveals that the energy of the backscattered projectile E_1 is fully determined by projectile mass M_1, target mass M_2 and scattering angle θ. During an experiment, the detector angle θ and the projectile mass M_1 are known, so the kinematic factor K solely depends on the target mass M_2. Hence, the notation K_{M_2}. The energy of the backscattered particles $E_1 = K_{M_2} E_0$ increases monotonically with increasing mass. Since we want to investigate the different masses present in the sample, the detector position is optimized to obtain the best mass resolution. This means that if different masses are present in the target, θ is chosen as such that a small change in target mass M yields a large change in K value. The largest change in K is for the detector at $\theta = 180°$. In practice detectors are positioned at $\theta = 170°$.

He projectiles will not only scatter from atoms at the surface of the material, various ions will penetrate into the target and will only be backscattered at a depth t as is illustrated in figure 2.3. For the projectiles shown in figure 2.3,

their energy E_1 when reaching the detector consists of three parts:

- Energy loss along the inward path due to inelastic scattering with electrons. The energy loss per unit depth $\frac{dE}{dx}$ varies as a function of E. For thin films, $\frac{dE}{dx}$ can be approximated by the value for $\frac{dE}{dx}$ at the energy E_0 (surface energy approximation)
- Nuclear energy loss caused by the backscattering event.
- Electronic energy loss along the outward path. When using the surface energy approximation, $\frac{dE}{dx}$ is approximated by the value of at the energy KE_0.

Based on figure 2.3, we can deduce a linear relationship between the energy loss of the backscattered particle and the depth t.

$$\Delta E = \Delta t \; [S_0] \tag{2.5}$$

ΔE is the energy difference between a particle scattered from a mass M_2 positioned at the surface and the mass M_2 positioned at a depth t. $[S_0]$ is given by the following

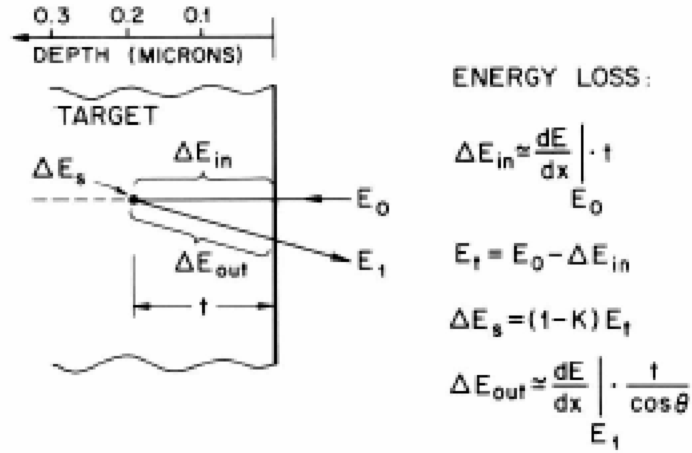

Figure 2.3: Energy loss during RBS. The projectile loses energy on the inward path ΔE_{in}, during the collision ΔE_S and on the outward path ΔE_{out} [44].

equation

$$[S_0] = \left[K \left[\frac{dE}{dx} \right]_{E_0} + \frac{1}{\mid \cos\theta \mid} \left[\frac{dE}{dx} \right]_{KE_0} \right] \tag{2.6}$$

in which $\frac{dE}{dx}$ has been considered constant as a function of the depth i.e. along the inward path given by the value for $\frac{dE}{dx}$at the energy E_0 and along the outward path given by the value for $\frac{dE}{dx}$at the energy KE_0. This approximation is called surface energy approximation. Mostly, the values for $\varepsilon = \frac{1}{N}\frac{dE}{dx}$are tabulated for a wide energy range in textbooks such as [42]. Hence, by measuring the energy difference ΔE, as drawn in figure 2.3, the thickness of the thin film can be determined via the stopping cross section ε.

2.2.2 Backscattering yield - Scattering cross section

Above, a description has been given of the different components influencing the energy of the backscattered projectile and how this is related to the depth of the scattered. Here, the scattering cross section or the probability that a particle will be scattered at a certain angle will be discussed. From the amount of backscattered particles at a certain energy, the concentration - depth profile can be obtained.

The number of particles that will be detected in a detector with solid angle Ω is given by

$$Y = \sigma(\theta) \Omega Q N_s \tag{2.7}$$

with N_s the number of target $atoms/cm^2$, Q the total number of incident particles in the beam, Ω is the detector solid angle and $\sigma(\theta)$ is the scattering cross section. The

scattering cross section $\sigma(\theta)$ is the probability that a particle will be backscattered in a detector solid angle , positioned at an angle θ . For RBS, this scattering cross section can be approximated by the Rutherford scattering cross section

$$\sigma(\theta) = \left[\frac{Z_1 Z_2 e^2}{4E}\right]^2 \frac{1}{\sin^4\left(\frac{\theta}{2}\right)} \tag{2.8}$$

As can be seen in the above formula, with Z_2 the atomic number of the target atom. Hence, for heavy masses (e.g. Fe $Z_2 = 26$), is much higher than for light targets (e.g. Si with $Z_2 = 14$). This is why the signal of Fe is much higher than that of the Si in the film though the amount of silicon is almost twice that of Fe. An estimate of the amount of Fe $atoms/cm^2$ present in a thin $FeSi$ 1 : 2 layer on a substrate can be obtained using the following equation [43]

$$N_{imp} = \frac{A_{imp}\sigma_{sub}\xi}{H_{sub}\sigma_{imp}\left[\varepsilon_0\right]_{sub}} \tag{2.9}$$

in which, A_{imp} is the integral of the Fe signal in the $FeSi$ 1 : 2 layer, H_{sub} is the height of the substrate signal near the surface. ξ is the energy width of a channel ($eV/channel$) and ε_0 is the stopping cross section.

$$[\varepsilon_0]_{sub} = \left[\frac{K}{\cos\theta_1}\varepsilon(E_0) + \frac{1}{\cos\theta_2}\varepsilon(KE_0)\right] \tag{2.10}$$

θ_1 and θ_2 are the angles between the surface normal and the incoming and outgoing beam respectively. K is calculated using the surface energy approximation as mentioned in section 2.2.1.

2.3 X-ray diffraction

The normal state of solid is the crystalline state. In a crystal the atoms occupy well-determined, fixed position in relation to each other. The ordinate microscopic structure will also be reflected in the macroscopic structure of the crystal conferring to it certain symmetry: symmetry axes, centre and planes.

Most solid substances are polycrystalline consisting of a compact agglomeration of crystals of small dimensions having nearly perfect crystallinity due to the random orientation of the crystallites, these materials are isotropic. Cases exist in which the crystallite have a preferred orientation as a consequence of a processing procedure.

2.4 Bragg's law

By the interaction of an electromagnetic radiation beam with the material, secondary radiations occur, some of which have the same frequency as of the incident beam

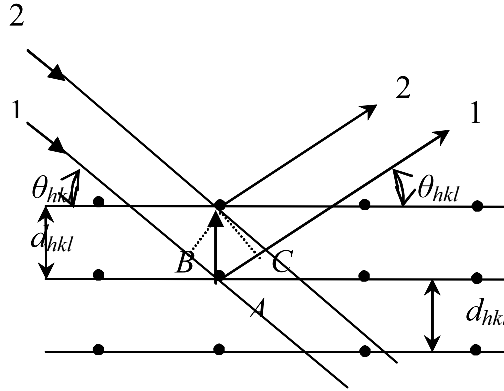

Figure 2.4: Diffraction of coherent beam on a set of planes

(coherent diffusion). As with visible radiation, coherent radiation makes possible the occurrence of the interference phenomenon.

If a plane, monochromatic X wave meets a crystal lattice, then the condition that the diffracted beam is intensified is given by Bragg's law (figure 2.4)

$$2d_{hkl} \sin \theta_{hkl} = n\lambda \tag{2.11}$$

when $AB + AC = n\lambda$

In relation (2.11) the diffraction order is included in the Miller indices of the set of planes[47].

From macroscopic measurement of the angle θ, the Bragg's relation permits data to be obtained concerning the characteristics of crystal lattices (d_{hkl}), a microscopic quantity. By completely interpreting the diffract ion patterns, taking into account the intensities of diffraction lines, all parameters of the crystal lattices can be determined.

In most application, the materials examined are polycrystalline, their small crystals being in a random or preferred orientation. For a random orientation the diffraction pattern exhibits a circular symmetry with respect to the incident beam. A preferred orientation is reflected in the distribution of the diffracted beam intensity around the circumference.

When we measure Bragg angles in a powder or polycrystalline specimen, we use goniometers with which the angle between the primary beam and the reflected beam (2θ) is determined.We do not care about the angle between the primary beam and the lattice plane since we know that only grains in the appropriate orientation contribute to the reflected beam. We only keep the specimen's surface in a symmetric position

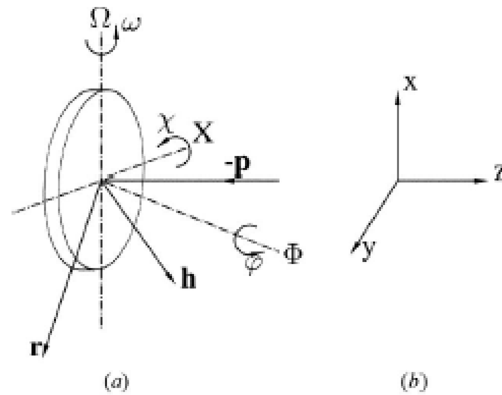

Figure 2.5: Outline of (a) the goniometer axes and (b) the coordinate system.

with respect to the primary and the reflected beam (the Bragg–Brentano geometry), but this is not crucial to the accuracy. In single crystals, the situation is quite different. If we again use a $\theta/2\theta$ goniometer, we must keep the reflecting lattice plane exactly in the symmetric position, which is not an easy task and if not done properly can cause errors. A simple and elegant solution of the problem was presented by Bond (1960)[46]. In his method, two rocking curves are recorded. The positions of the specimen where the lattice plane is in its best reflecting position are determined, and from the two rocking curves the Bragg angle θ is obtained. A further great advantage of Bond's method compared with the $\theta - 2\theta$ geometry is that it needs virtually no alignment of the whole goniometer. There is only one disadvantage, namely one must have a special goniometer or at least adapt a standard goniometer.

Consequently, Bond's method is not used very often in single-crystal stress measurements. Therefore, another method is proposed which is also based on rocking curves but can be performed with a standard goniometer equipped with an Eulerian cradle. (In stress measurements, whether of single-crystalline or polycrystalline materials, an Eulerian cradle is always necessary.) The new method also presents a disadvantage: it requires an additional alignment procedure or, instead, the measurement of a standard specimen. However, the measurement of a standard is easily and quickly done, and single crystals of high quality and well known lattice constants (measured with Bond's method) are readily available.

Nomenclature

Figure 2.5 shows an outline of an Eulerian cradle and, parallel to it, a fixed laboratory system.

p is the negative direction of the primary beam. p is parallel to the z axis.

h is the vector normal to the reflecting plane.

r is the reflected beam.
$\boldsymbol{\Omega}$ is the Ω axis, parallel to the x axis.
X is the X axis, parallel to the z axis when $\omega = 0$.
$\boldsymbol{\Phi}$ is the Φ axis, parallel to the y axis when $\omega = 0$ and $\chi = 0$.
All rotations are in the positive sense with regard to the coordinate system (see figure 1a).
$\boldsymbol{\theta}$ is the exact Bragg angle.
$\boldsymbol{\theta}'$ is the measured Bragg angle.

2.5 Transmission electron microscopy (TEM)

In the studies described in this thesis, the TEM analysis was performed in a Philips $CM300$ operating at $300KV$.

The wave nature of the electrons is used in transmission electron microscope in order to visualize features which are too small to be observed in the optical microscope. A beam of electrons is accelerated by a high voltage ($> 100KV$), passes through the sample, as well as through a set of apertures and electromagnetic lenses and creates an image of the sample on, e. g., a fluorescent screen. The objective lens, placed after the sample holder (figure 2.6), produces a picture of the reciprocal space of the sample, in its back focal plan and the real picture of the sample in its image plane. Further projection of either the back focal plane or the image decides whether the image on the screen is a picture of the real or the reciprocal space.

There are two important mechanisms, which produce image contrast in the electron microscope.

2.5.1 Diffraction contrast

In the bright field imaging (BF), diffracted leaving the lower surface of a crystalline specimen are intercepted by the objective aperture inserted in the back focal plane and prevented from contributing to the image (see figure 2.6a). Alternatively only one diffracted beam forms the image in the dark field (DF) mode (see figure 2.6b). Bright field is the mostly used imaging mode in this study. DF mode was used as a part of a technique to determine the nature of defects. The diffraction (Bragg) contrast of crystalline specimens is caused by the elastically diffracted electrons in Bragg reflections. The interpretation of the TEM images is explained by the dynamical theory of the electron diffraction[47]. Electron beams interact strongly with the atoms in a crystal, and any beam can easily be scattered more than ones, i.e. a beam which has been diffracted can be rediffracted. Any electron beam that is oriented at the Bragg

angle is ideally oriented to be rediffracted. Dynamical diffraction theory deals with interaction between primary and reflected electron beams. When the Bragg condition is only met for one point in the reciprocal lattice or one diffraction vector g (usually along [110] −zone axis of Si, used in this study), a two-beam case results, and the primary and reflected beams oscillate in intensity with increasing crystal thickness. If the Bragg condition is met exactly the so called excitation error is equal to zero, this is a dynamical case. When the Bragg condition is met only approximately (excitation error <0 or >0), this is the so called kinematical case.

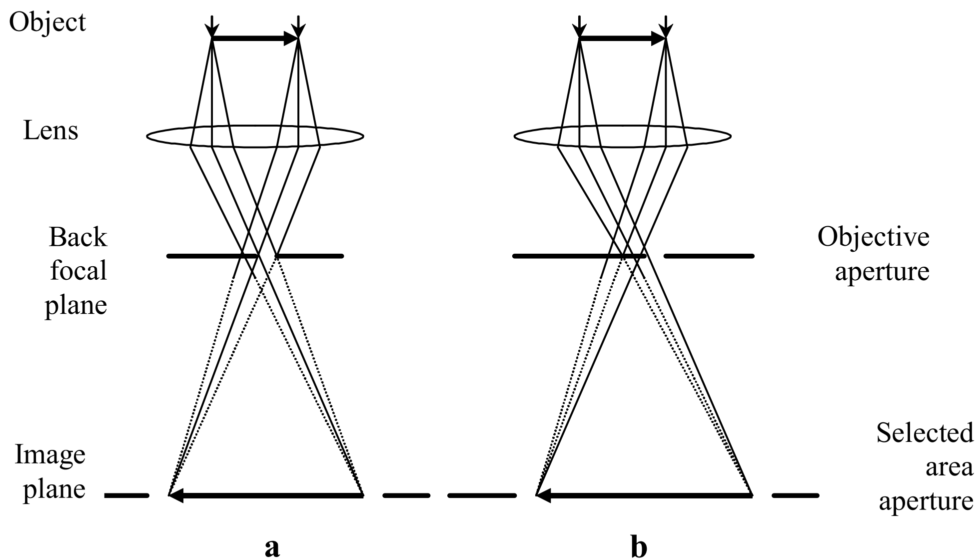

Figure 2.6: Ray diagrams showing the principles of formation of (a) BF contrast and (b) DF contrast. The dashed rays will not contribute to the final image.

2.5.2 Phase contrast

Some of electrons leaving the specimen are recombined to form the image so that the phase differences present at the exit surface of the specimen are converted into intensity difference s in the image.

In transmission electron diffraction, the reciprocal space patterns in the back focal plane of the objective lens are projected down to the screen. Mostly used is the technique of selected area electron diffraction (SAED)[48], where a selected area aperture is inserted in the image plane of the objective lens (see figure 2.5b). This is done to shield certain areas of the sample, i.e., only electrons which have passed a chosen

sample area will give intensity to the different patterns. In the work presented in this thesis, the SAED was used to orient the sample in a way that certain crystallographic direction is parallel to the electron beam.

An important part of TEM investigation is the specimen preparation. Bulk samples must be prepared for viewing in the TEM so that they became transparent for electrons. Typical thickness of $100nm$ or below have to be employed. Obtaining specimens thin enough and containing the defects to be investigated in the right geometry (e.g. in cross section XTEM) is a crucial point in the TEM studies. In what follows the XTEM specimen preparation techniques that where used for the preparation of the samples investigated in the study will be described.

2.6 TEM specimen preparation by ion-milling

The XTEM specimens were prepared conventionally by cutting 2 stripes ($2\times3mm$) of the material and gluing face-to-face. A dummy Si material was glued to both rear sides of the original material till the thickness of the "sandwich" became 3 mm in order to cut a disk with a diameter of $3mm$. The disk contains the range of interest (see figure 2.7a) which is standard size used of the TEM microscopy holders. Mechanical thinning of the specimen was performed by grinding to get a disk with flat plane-parallel surfaces (thickness $\sim 0.2mm$). As a next step, the sample was dimpled till the central area has thickness of about $5 - 10\mu m$. For the final thinning the sample was subsequently ion-milled. Ion-milling is a TEM sample preparation technique where the sample material is typically bombarded by argon ions. Thereby material is removed away to cause a small perforation in the middle of the sample in the region of interest. The thinning of the specimen is achieved by sputtering of the near surface atoms of the sample during argon bombardment (see figure 2.7b) performed almost always using commercial ion-milling machines. Due to this ion-milling procedure it is possible to achieve a large, uniform thin area in the centre of the sample (thickness $< 100nm$), which is electron-transparent. The thinning process can be prolonged until a hole is generated.

The sputtering yield, defined as a ratio of the mean number of the emitted atoms to the flux of the incident particles depends on the energy of the incident particles, i.e., ions and neutrals; the angle of incidence of the sputtering beam θ, the relative masses of the specimen atoms and incident particles, the characteristics of the material as the mass and the cohesive energy of the sputtering target. Other factors influencing the sputtering yield are the specimen temperature, the concentration and chemical nature of any background gases, the crystallinity of the specimen, any chemical interactions occurring between the incident particles and the specimen, and specimen

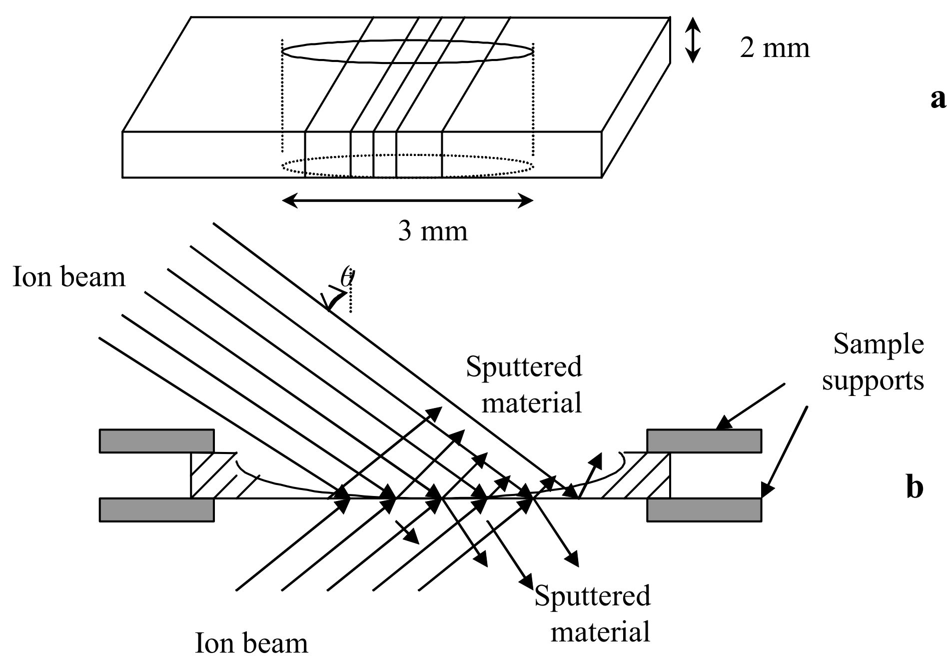

Figure 2.7: Scheme of cross-section TEM sample preparation: (a) two stripes of material containing areas of interest are glued face-to-face,(b) the sample is dimpled on the upper side and ion-milled from both sides.

contamination. The ion-milling process has the effect of producing surface damage, i.e. amorphization. This effect is extremely undesirable when sputtering is used for the final thinning of the XTEM specimen. The presence of the thick amorphous layer $(7 - 10nm)$ on the surface of the TEM specimen reduce the resolution of the TEM imaging. All above mentioned parameters have to be optimized in order to achieve a reasonable sputtering yield while causing minimum thickness of the amorphous layer on the surface of the specimen. The range of the available accelerating voltage of Ar^+ ions amounts to ˜ $0.1 - 10KeV$ (depending on the manufacturer), but the samples with least damage are prepared at voltages lower than $4KeV$. One of the widely used conventional ion-milling machine is the "Due Ion Mill 600" produced by GATAN Inc. In this machine ion-milling can be performed under milling angles in the range of $70° + 80°$. It was used for the preparation of a part of a Si specimens that were investigated in this work. The milling parameters for the Si substrates were: $4KeV$ Ar^+ ions, $1mA$ total current at incidence angles of $\theta = 73°, 75°$ and $77°$. There are no references found in the literature which show that the ion milling performed in this machine induces any modification of the real structure of the sample.

In recent years one can observe a trend to increase the milling angle θ in order to minimize the specimen surface damage. The new generation ion-milling system "PIPS" by GATAN has the capability of increasing θ to values higher than $85°$, in this way decreasing the amorphisation of the TEM specimen surface.

In order to increase the probability for TEM imaging of the $R_p/2$ defects, i.e. very small defect complexes, a special effort was made to improve the quality of the XTEM specimens in respect of decreasing the amorphous surface layer, and to avoid the use of any treatment during the XTEM sample preparation which can modify the defect structure needed to be investigated. As an alternative to the conventional XTEM specimen preparation by ion milling, the cleavage technique was used in the $R_p/2$ effect, related studies are reported in this thesis.

2.7 TEM specimen preparation by cleavage

Cleavage is a technique for producing cross-sectional TEM specimens of crystalline materials such as semiconductor substrates. "Cleavage" refers to the separation of a crystal along specific atomic planes [49]. When sufficient stress is applied to a silicon crystal, it will typically cleave along a plane which requires the fewest bonds to be broken. The (111) planes are preferred cleavage planes in Si crystal as there is the lowest number of bonds, n, in these planes - $n(111) = 7.83 bonds/nm^2$compared to the (110) planes - $n(110) = 9.59 bonds/nm^2$, and (120) planes - $n(120) = 12.14 bonds/nm^2$. For the case of $[111]Si$ oriented wafer the set of the planes used for cleaving are (-110)

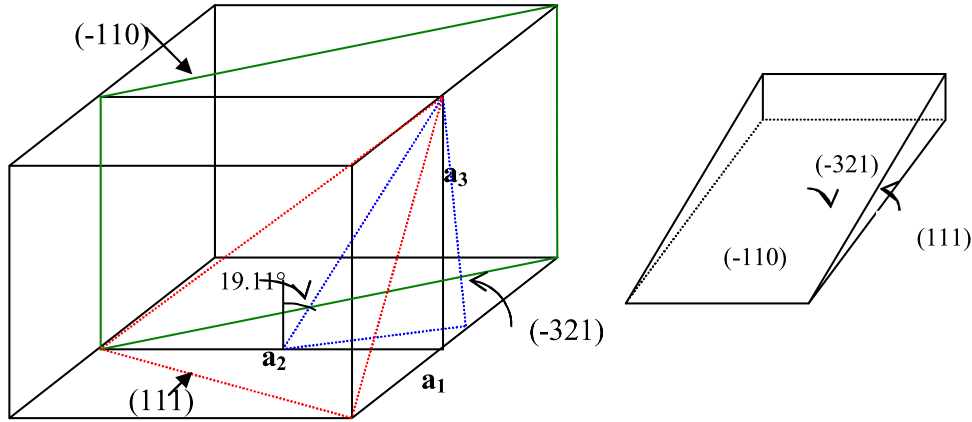

Figure 2.8: Cleavage plane orientations for $[111]Si$ wafer; a_1, a_2 and a_3 are the vectors of the unit cell.

and (-321). The plane orientations and the scheme of the resulting wedge are shown in figure 2.8.

2.8 Electron diffraction

A parallel monochromatic electron beam may be considered to be equivalent to plane wave of wavelength λ. At the accelerating voltages used, λ is usually much less than d, so the Bragg relation may be written in a simplified form

$$2d_{hkl}\theta \approx \lambda \tag{2.12}$$

An interplanar spacing $d = 1\mathring{A}$ and an accelerating voltage of $100KeV$ gives an angle of incidence of $\theta \approx 1°$.

If the material used for diffraction is crystalline and unoriented, then, as in the case of X-rays, the directions satisfying the Bragg relation exhibit a circular symmetry with respect to the direction of the incident beam. For various interplanar spacings a family of cones is obtained, having the tip at the point of contact between the electron beam and the specimen. The intersection of these cones with a plane surface generates a characteristic diffraction pattern, in the form of concentric rings.

As the angle 2θ is small, the radius of a diffraction ring may be written approximately $R = 2\theta L$, where L is the distance from the specimen to the photographic plate. Replacing the value for the angle θ in the preceding relation by the simplified equation a simple interdependence is obtained between the interplanar spacing, the diffraction

ring radius R, and the instrument characteristic L

$$d_{hkl} = \frac{\lambda L}{R} = \frac{K}{R} \tag{2.13}$$

The constant K of the instrument may be determined from the optical system characteristics and the wavelength used.

Part II: Experimental details

2.9 Experimental details

An iron silicide layer was produced by $195KeV$ Fe^+ ion implantation with a dose of $2 \times 10^{17} Fe^+/cm^2$ into a chemically cleaned p-type $Si(111)$ wafer with a high current implanter from the DANPHYSIK A/S. The beam current was $11\mu A/cm^2$ scanned over 2x2 cm^2 area. During the implantation the substrate was heated at T_i = 500 $°C$. After implantation, the samples were annealed in a N_2 atmosphere at 850$°C$ and 1000$°C$ for 90min. The implantation conditions led to the formation of both β-phase and α-phase and the recrystallization of ion beam damaged Si substrates. Rutherford backscattering spectrometry (RBS) was performed with 1.7 MeV He^+ ions at a scattering angle of 170° between the incoming and outgoing beam line and the experimental spectra were analyzed with the RUMP computer program [50]. XRD pole figure measurements were performed by the following diffractometers:

1) D5000 (Siemens / BrukerAXS) using Cu-K$_\alpha$ radiation λ = 0.154nm (High voltage 40kV, current 30mA) / Entrance slit 1mm x 15mm / focusing multilayer mirror with exit slit 1mm x 15mm / sample / soller slits and secondary graphite monochromator / Scintillation detector, a diffractogram is measured in the range 2θ = 15.0° (0.1°) 70.0° at an incidence angle of 0.5 ° with 30s measuring time per point.

2) D5005 (Siemens / BrukerAXS) with $\frac{1}{4}$ circle Eulerian cradle using $Cu-K_\alpha$ radiation $\lambda = 0.154nm$ (High voltage 40kV, current 30mA) / Entrance slit 1mm x 1.2mm / focusing multilayer mirror with exit slit 1mm x 1.2mm / sample / antiscattering slit 2mm x 15mm / detector slit 2mm x 5mm / scintillation detector: A diffractogram is measured in the range 2θ= 14.00° (0.05°) 80.00° in Bragg Brentano geometry with 20s measuring time per point: Pole figures are measured with steps of 5° in φ and χ angles.. The structure of the buried layers was studied by cross-section XTEM using a Philips CM 30 microscope with 300KV acceleration voltage.

2.10 Results and discussion

Figure 2.9a shows the RBS spectrum of (111)Si sample in the as-implanted state with an ion dose of 2x10^{17} Fe^+/cm^2at a substrate temperature of 500$°C$, obtained in the random direction. As can be seen, the Si signal reaches the surface position, and the depth profile obtained by RUMP simulation is shown in figure 2.9b. The RBS spectrum indicates the formation of thin $FeSi_2$ buried layer (62nm).

The RBS spectra of samples implanted at T_i = 500$°C$ and annealed in a N_2 atmosphere at 850$°C$ and 1000$°C$ for 90min, are shown in figure 3.2. By increasing the temperature treatment, the height of Fe signal decreases whereas the energetic

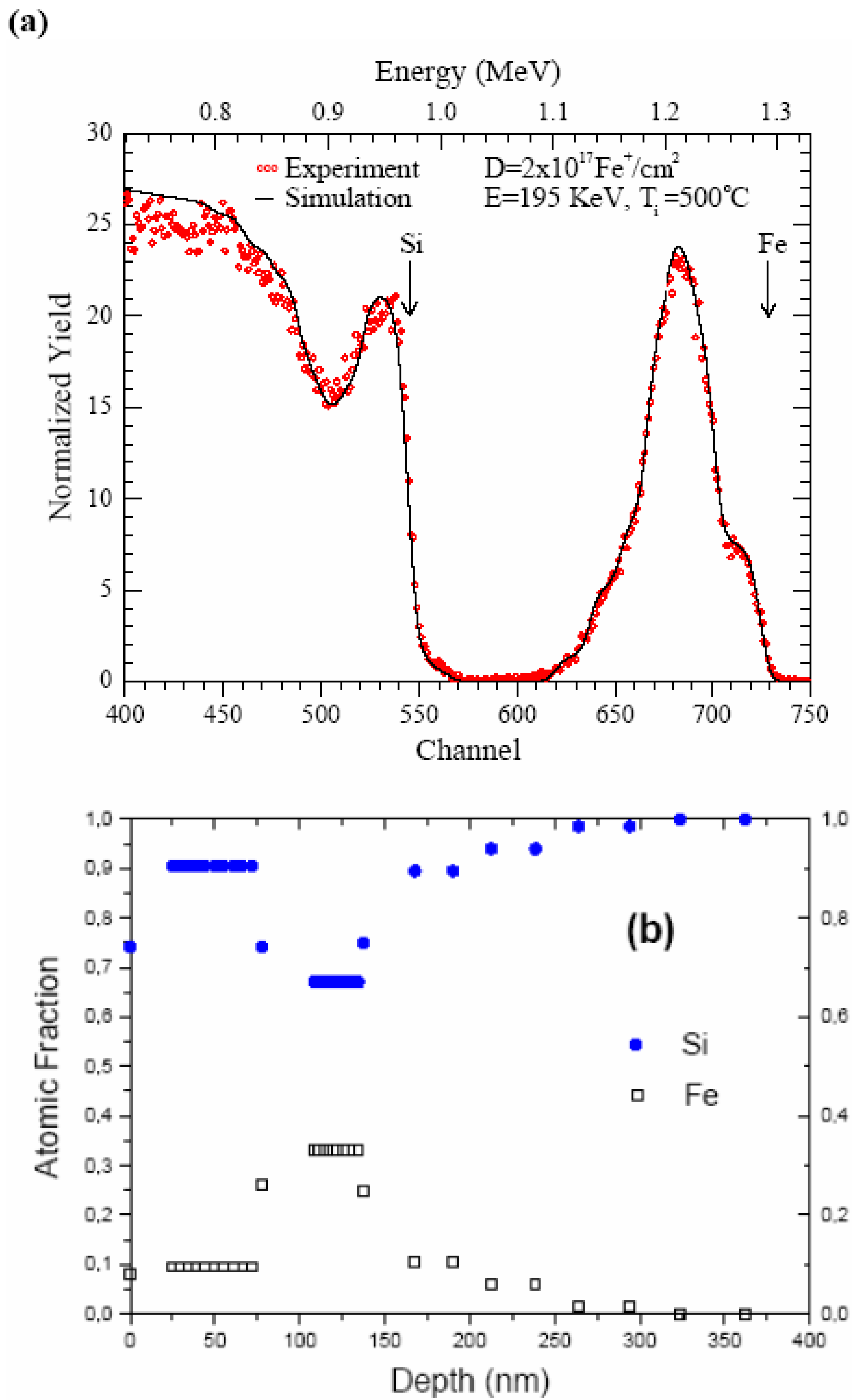

Figure 2.9: (a) RBS spectrum of $195keV$ Fe ion implanted $(111)Si$ substrate at $500°C$ with a dose of $2x10^{17}Fe^{+}/cm^{2}$. $(b)Fe$ depth profile deduced from (a).

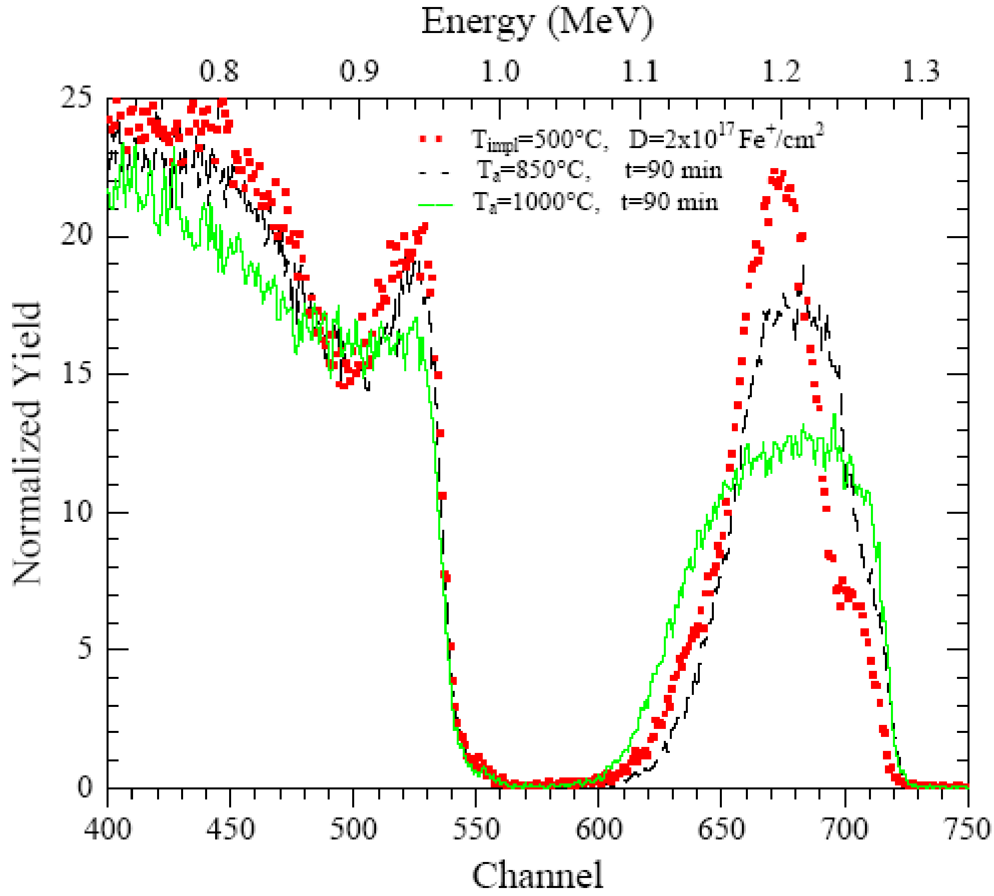

Figure 2.10: RBS Random spectra of 195 KeV Fe^+ implanted into $(111)Si$ substrate with a dose of 2x10^{17} Fe^+/cm^2 for as-implanted and subsequently annealed samples in a N_2 atmosphere during 90min at 850°C and 1000°C.

width increases (figure 2.10). In the same time, the Si signal, around channel 500, corresponding to the buried $FeSi_2$ layer is extended to the surface. The analysis of the spectra using the RUMP program indicates that the thickness of $FeSi_2$ layer increases from 62nm to about 92nm and 145nm after annealing at 850°C and 1000°C respectively.

Figure 2.11a shows the XRD pole figure of the sample implanted with a dose of 2x10^{17} Fe^+/cm^2 at $T_i = 500°C$ and annealed in a N_2 atmosphere at 850°C for 90min. As can be seen, the $\beta - FeSi_2$ crystals are oriented in the Si substrate; the poles with heights of 10.93, 24.28, 17.29, 21.68 and 5.49 are produced by the tails of the $(111)Si$ reflections (its maximum is located at $2\theta = 28.443°$) of the substrate. They give the orientation of the substrate. The poles with the heights of 19.50, 16.30

and 34.37 near the centre and at scattering angle $2\theta = 29.112°$ in the periphery are $(220)\beta - FeSi_2/(202)\beta - FeSi_2$ reflections. As a result, the epitaxial relationship is described as follows: $(220)\beta - FeSi_2$ and/or $(202)\beta - FeSi_2//(111)Si$. Partial pole figures of the $(101)\alpha - FeSi_2$ reflections (not shown) at the scattering angle $2\theta = 37.668°$ and of the (220) and/or $(202)\beta - FeSi_2$ reflections at the scattering angle $2\theta = 29.112°$ are measured with steps of 5° of φ and χ angles (φ and χ are the azimuth and rotation axes perpendicular to the substrate, respectively) in the whole range of φ and in the range χ=35-40° of three $\beta - FeSi_2$ poles. It is worth noting that only a very small amount of $\alpha - FeSi_2$ phase was found in both samples (as-implanted at $500°C$ and annealed in a N_2 atmosphere at $850°C$ for $90min$). The figure 2.11b shows a typical XRD spectrum at the pole position of 'Z' in figure 2.11a. Figure 2.11c presents the partial pole figure of $\alpha - FeSi_2$ reflections measured in the whole range of φ and χ=35-45° at the scattering angle 2θ=37.668° of the sample annealed in a N_2 atmosphere at $1000°C$ for $90min$. The six poles near the centre with the heights of 92.33, 129, 253.81, 107.10, 78.15 and 59 are $(101)\alpha - FeSi_2$ reflections; the poles with the heights of 4.79, 4.41, 10.95, 2.24, 2.01 and 3.56 are produced by the tails of the $(111)Si$ reflections. They give the orientation of the substrate. In this case the epitaxial relationship is $(101)\alpha - FeSi_2//(111)Si$. This result shows clearly that the transformation from $\beta - FeSi_2$ to $\alpha - FeSi_2$ has occurred after annealing at $1000°C$ for $90min$. However, the XRD analysis shows that a small amount of beta phase persists. As suggested previously by D. Panknin et al. [51], the transformation from $\beta - FeSi_2$ to $\alpha - FeSi_2$ by annealing at $1000°C$ occurs very rapidly, because $\alpha-$ phase has a lower iron concentration than $\beta-$ phase. The excess iron diffuses to the interface of the silicide layer and forms additional $\alpha-$ phase resulting in an increased width of the silicide. To our knowledge, $\alpha - FeSi_2$ has a simple tetragonal lattice structure with only three atoms in unit cell and a small lattice mismatch with the Si matrix [52].

The cross-section TEM observation of the as-implanted sample is presented in Figure2.12a. The Si top layer, a continuous buried $\beta - FeSi_2$ layer, and the Si substrate are indicated. The $\beta - FeSi_2$ phase is deduced from transmission electron diffraction (TED) (not shown). As can be seen, at the top and the bottom of the buried layer, there are many small precipitates of the $\alpha - FeSi_2$ and $\beta - FeSi_2$ with different morphology and sizes which are identified by microdiffraction. We notice that the interfaces of the buried layer are not flat . The microstructure of the same sample annealed at $850°C$ for $90min$ is shown in figure 2.12b. The examination of the continuous layer confirms that, after this heat treatment, the nature of the buried layer is not modified yet ($\beta - FeSi_2$). However, the buried $\beta - FeSi_2$ layer becomes more homogeneous and flat with a thickness of about $100nm$. Also, we observe variations in

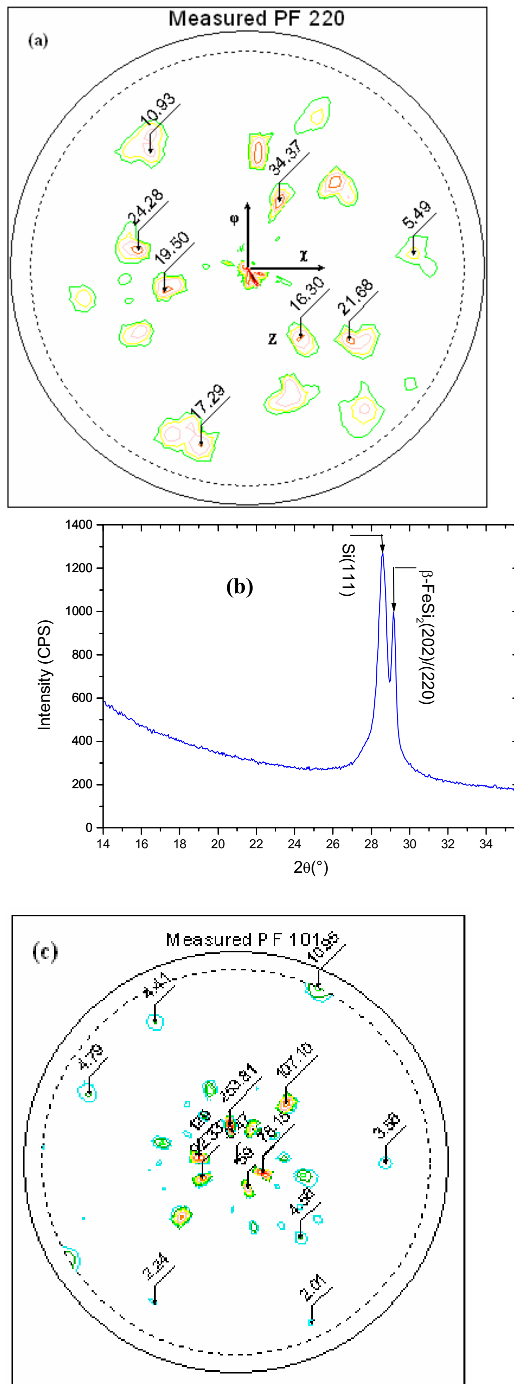

Figure 2.11: (a) X-ray pole figure plot of (220) diffraction peak of $\beta - FeSi_2$ and (111) Si for the sample implanted and annealed at 850°C for 90min. (b) XRD Spectrum scanning at the pole position of point 'z' in figure 2.9(a). (c) Partial pole figure of the (101)$\alpha - FeSi_2$ reflections at the scattering angle 2 θ=37.668°

size and shape of the small grains (precipitates). Indeed, all precipitates have become appreciably larger and highly facetted, and their density decreases.

2.11 Conclusion

Implantation of $195KeV$ Fe^+ with a dose of $2x10^{17}$ $at./cm^2$ in $(111)Si$ substrates at $500°C$ followed by annealing at $850°C$ for $90min$ allows the formation of a continuous buried $\beta - FeSi_2$ layer. The buried layer is grown epitaxially on $(111)Si$ substrate with the relation of (220) and / or $(202)\beta - FeSi_2//(111)Si$. A mixture of $\beta - FeSi_2$ and $\alpha - FeSi_2$ is observed. After annealing at $1000°C$, the study shows the transition from $\beta - FeSi_2$ to $\alpha - FeSi_2$, and the main epitaxial relationship found is $(101)\alpha - FeSi_2//(111)Si$.

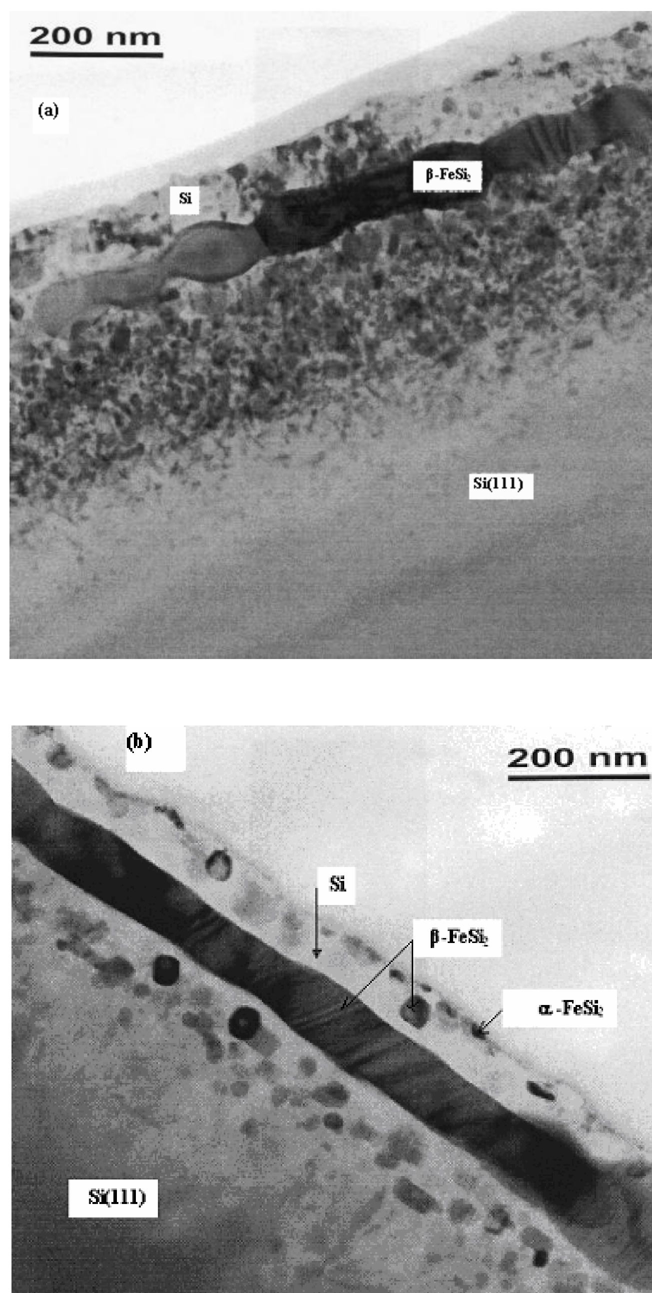

Figure 2.12: Cross-sectional TEM images of 195 KeV Fe^+ implanted $(111)Si$ substrate at $500°C$ with a dose of 2x10^{17} Fe^+/cm^2 : (a) as-implanted, (b) annealed in a N_2 atmosphere at $850°C$ for $90min$.

Chapter 3

Optical characterization

3.1 The Raman Effect

When electromagnetic radiation of energy $h\nu$ content irradiates a molecule, the energy may be transmitted, absorbed, or scattered. In the Tyndall effect the radiation is scattered by particles (smoke or fog, for example). In Rayleigh scattering the molecules scatter the light. No change in the wavelength of individual photons occurs in either Tyndall or Rayleigh scattering[53].

In Raman spectrometer the sample is irradiated with an intense source of monochromatic radiation usually in the visible part of the spectrum. Generally this radiation frequency is much higher than the vibrational frequencies but is lower than the electronic frequencies. The radiation scattered by the sample is analyzed in the spectrometer. Rayleigh scattering can be looked on as an elastic collision between the incident photon and the molecule. Since the rotational and vibrational energy of the molecule is unchanged in an elastic collision, the energy and therefore the frequency of the scattered photon is the same as that of the incident photon. This is by far the strongest component of the scattered radiation. The Raman effect can be looked on as an inelastic collision between the incident photon and the molecule where as a result of the collision the vibrational or rotational energy of the molecule is changed by an amount ΔE_m . In order that energy may be conserved, the energy of the scattered photon, $h\nu_s$, must be different from the energy of the incident photon $h\nu_i$, by an amount equal to ΔE_m:

$$h\nu_i - h\nu_s = \Delta E_m \tag{3.1}$$

If the molecule gains energy then ΔE_m is positive and $h\nu_s$ is smaller than $h\nu_i$, giving rise to Stokes lines in the Raman spectrum. This terminology arose from Stokes

rule of fluorescence which states that fluorescent radiation always occurs at lower frequencies than that of exciting radiation. If the molecule loses energy, then ΔE_m is negative and $h\nu_s$ is larger than $h\nu_i$, giving rise to anti-Stokes lines in the Raman spectrum.

In figure 3.1 the difference between two levels is given by $\Delta E_m = h\nu_m$ A transition directly between these two levels causes the absorption of an infrared photon whose frequency is the same as the molecular frequency ν_m. In Rayleigh and Raman scattering, the frequency of the incident photon is usually greater than ν_m. When the incident photon interacts with a molecule in the ground vibrational state $\upsilon = 0$,the molecule absorbs the photon energy and is raised momentarily to some high level of energy (dashed line) which is not a stable energy level. Therefore, the molecule immediately loses energy and, most probably, returns to the ground vibrational level, emitting a scattered photon (to make up for its energy loss) whose energy and frequency is the same as that of the incident photon. This is Rayleigh scattering. However, a small proportion of the molecules in the instable high level of energy may fall, not to the ground vibrational level but to the $\upsilon = 1$ energy level. The scattered photon in this case has less energy than the exciting photon, the difference being

$$h\nu_i - h\nu_s = \Delta E_m = h\nu_m \tag{3.2}$$

so $\nu_s = \nu_i - \nu_m$ when $\Delta\upsilon = +1$

This scattered photon gives rise to a Stokes line in the Raman spectrum. According to quantum mechanics the allowed change in the vibrational quantum number for the Raman transition is $\Delta\upsilon = \pm 1$ for a harmonic vibration. The final possibility is that initially is in the excited state $\upsilon = 1$, absorbs the incident photon energy, and is raised to an unstable high level energy. When the molecule falls to the ground vibrational level $\upsilon = 0$, the energy loss is made up by the emission of photon whose energy is greater than that of the incident photon by $h\nu_m$. This scattered gives rise to an anti-Stokes line in the Raman spectrum[54].

3.2 Polarizability

The polarizability can be looked on as the deformability of the electron cloud of the molecule by the electric field. In order for a molecular vibration to be Raman active, the vibration must be accompanied by a change in the polarizability of the molecule.

The electric field of the electromagnetic radiation in the vicinity of the molecule varies with time so that

$$E = E_0 \cos 2\pi\nu t \tag{3.3}$$

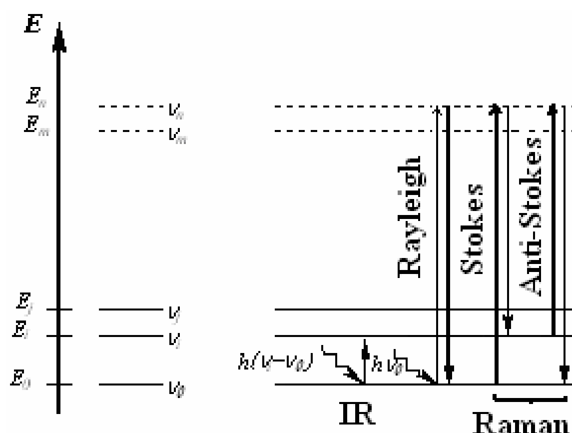

Figure 3.1: Schematic illustration of Raman and Rayleigh scattering and infrared absorption

where E_0 is a constant, the maximum value of the field, ν is the frequency of the radiation, and t is time. This oscillating electric field will induce in the molecule an oscillating dipole moment μ whose frequency will be the same as that of the external electric field. The dipole moment is given by:

$$\mu = \alpha E \tag{3.4}$$

where α is polarizability. Combining $Eqs.$(3.3)and (3.4), we get

$$\mu = \alpha E_0 \cos 2\pi\nu t \tag{3.5}$$

From classical theory this oscillating dipole moment will emit radiation in all directions having the same frequency as that of the oscillating dipole moment, and whose intensity is proportional to the square of the maximum value for μ, which $\alpha^2 E_0^2$ is in $Eq.$(3.5).

In molecules the polarizability α is not a constant since certain vibrations and rotations can cause α to vary. For small displacements the polarizability can be explained in the Taylor series as

$$\alpha = \alpha_0 + \frac{\partial\alpha}{\partial Q} + ... \tag{3.6}$$

where α is the equilibrium polarizability, Q is a normal coordinate (which is $r - r_0$ in diatomic case), and

$\frac{\partial\alpha}{\partial Q}$ is the rate of change of polarizability with respect to Q measured at the equilibrium configuration. Higher order terms are neglected in harmonic approximation.

The normal coordinate Q varies periodically

$$Q = Q_0 \cos 2\pi\nu_\nu t \tag{3.7}$$

where ν_ν is the frequency of the normal coordinate vibration and Q_0 is a constant, the maximum value for Q. Combining $Eqs.(3.6) and$ (3.7), we obtain

$$\alpha = \alpha_0 + \frac{\partial\alpha}{\partial Q} Q_0 \cos 2\pi\nu_\nu t \tag{3.8}$$

the substitution of this value for α into $Eq.$(3.5) yields

$$\mu = \alpha_0 E_0 \cos 2\pi\nu t + \frac{\partial\alpha}{\partial Q} Q_0 E_0 (\cos 2\pi\nu_\nu t)(\cos 2\pi\nu t) \tag{3.9}$$

It can be seen from this equation that the induced dipole moment μ varies with three component frequencies , $\nu, \nu - \nu_\nu$ and $\nu + \nu_\nu$ can therefore give rise to Rayleigh scattering, Stokes, and anti-Stokes Raman scattering, respectively. This classical prediction for these frequencies corresponds to the quantum mechanical result for Raman transitions when $\Delta\upsilon = \pm 1$. If the vibrations cause no change in polarizability so that $\frac{\partial\alpha}{\partial Q} = 0$, the $Eq.$(3.10) shows that the Raman component frequencies of the induced dipole moment have zero amplitudes and therefore no radiation with Raman frequencies can be generated.

The intensity of a Raman band depends on the polarizability of the molecule, the source intensity, the concentration of active groups, and other factors. Without absorption, the intensity of the Raman emission rises with the fourth potence of the source frequency. The Raman intensities are directly proportional to the concentration of active species. Since Raman lines represent frequency differences from the incident frequency, they are also called Raman shifts and are designated as $\Delta\nu$ in cm^{-1}. They are independent of the excitation wavelength. As a result, the anti-Stokes lines are weaker than the red shifted spectrum where they appear as Stokes lines. The ratio of the intensities of equivalent pairs of lines $I_{anti-Stokes}/I_{Stokes}$ falls as the vibrational frequency increases, and decreases with temperature.

Basically two types of Raman equipment can be described: Macro and micro-Raman. The former has the advantage of higher illumination region over the sample, being ideal for liquids and powder samples, and the disadvantage of the difficulty in focusing the specimen. The equipment used for both methods is basically the same, only a conventional optical microscope being added for micro-Raman spectroscopy.

A typical current Raman spectrometer incorporates (figure 3.2):

1) A macrosample chamber and a classical optical microscope for microanalysis.

2) A dispersive system composed of a double monochromator and a spectrograph.

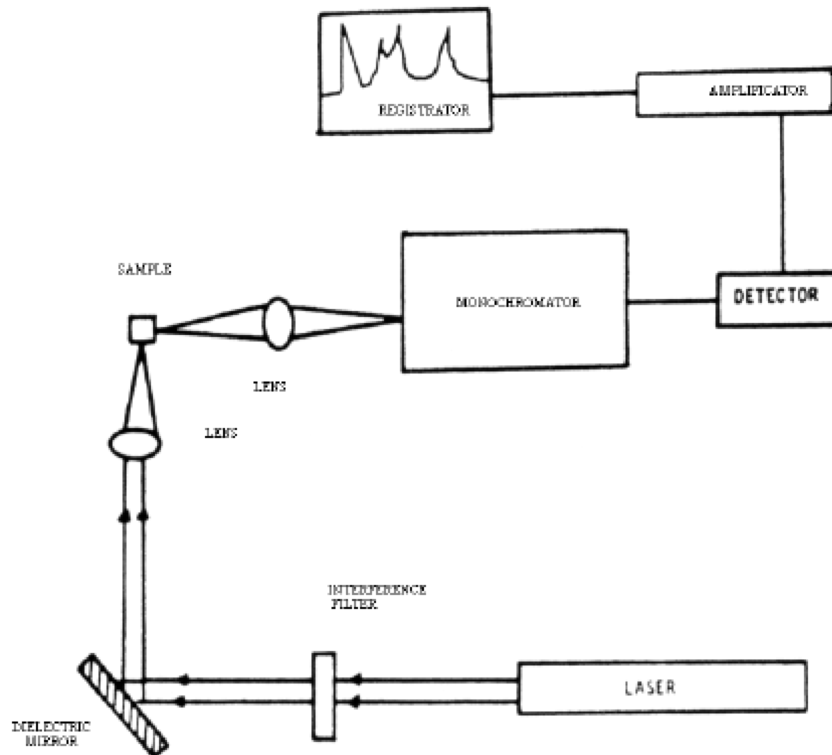

Figure 3.2: Schematic representation of a Raman spectrometer.

The two monochromators can be used either in subtractive mode to provide a wide field to the spectrograph or in additive mode when higher resolution is required. The double monochromator has one or two slits in between the first and second stage monochromators.

3) The detection system, which includes a multichannel detector (a linear diode array) and a photomultiplier connected to a single photon counter.

With point illumination the laser light is focussed on a sample surface by an objective lens and the scattered light is collected by the same objective. The spot size in the focal plane is diffraction limited. Although higher spatial resolution is obtained with this illumination method, heating or degradation of the samples by high density of laser powers can occur. Using a 100x objective, the spot size in the sample is about $0.4\mu m$ for $\lambda = 532.14nm$. This results in a very high power density in the specimen of the order of several mW/cm^2.

3.3 Infrared (IR) transmission and absorption spectroscopies

If I_0 is the intensity, or radiant power, of monochromatic radiation entering a sample, and I is the intensity transmitted by the sample, then the ratio $\frac{I}{I_0}$ is called the transmittance of the sample and is given by the symbole T. The percent transmittance ($\%T$) is equal to $100T$. If the sample cell has a thickness b, and the absorbing component has a concentration c, then the fundamental equation governing the absorption of radiation as a function of transmittance is

$$T = \frac{I}{I_0} = 10^{-abc} \tag{3.10}$$

The constant a is called the absorptivity and is a characteristic for a specific sample at a specific wavelength. This equation using transmittance is usually transformed by taking the logarithm to the base 10 of both sides of the equation and replacing $\frac{I}{I_0}$ with $\frac{I_0}{I}$ to eliminate the negative sign.

$$Log_{10}\frac{I_0}{I} = abc \tag{3.11}$$

The term $Log_{10}\frac{I_0}{I}$ is given the symbol A and is called the absorbance. The absorption law is commonly called Beer's law and usually written as function of absorbance as $A = abc$

The product of the concentration c and the thickness b, is a measure of the relative number of absorbing molecules in the infrared beam. The absorptivity a is constant specific for the substance at a particular wavelength and also varies with the units used for b and c. The absorbance A is alternately given by

$A = Log_{10}\frac{1}{T}$ or $A = Log_{10}\frac{100}{\%T}$

Beer's law is considered to be additive. In a mixture, the absorbance at a given wavelength or wavenumber is equal to the sum of the abc values for each component,

$$A = \sum_i a_i b c_i \tag{3.12}$$

Where the summation is over all the $\ddot{i}$ components present.

3.4 Fourier Transform Infra Red

Infrared spectroscopy is a very useful technique for characterisation of materials, not providing only information about the composition and the structure of molecules,

but also morphological information. The advantages of infrared spectroscopy include wide applicability, nondestructiveness, measurement under ambient atmosphere and the capability of providing detailed structural information. Besides these intrinsic advantages (of the known as dispersive infrared spectroscopy), the more recent infrared spectroscopy by Fourier transform (FTIR) has additional merits such as: higher sensitivity, higher precision (improved frequency resolution and reproducibility), quickness of measurement and extensive data processing capability (as FTIR is a computer based technique, it allows storage of spectra and facilities for processing spectra). IR spectra originate in transitions between two vibrational levels of a molecule in the electronic ground state and are usually observed as absorption spectra in the infrared region. For a molecule to present infrared absorption bands it is needed that it has a permanent dipole moment. When a molecule with at least one permanent dipole vibrates, this permanent dipole also vibrates and can interact with the oscillating electric field of incident infrared radiation. In order for this normal mode of vibration of the molecule to be infrared active, that is, to give rise to an observable infrared band, there must be a change in the dipole moment of the molecule during the course of the vibration. Thus, if the vibrational frequency of the molecule, as determined by the force constant and reduced mass, equals the frequency of the electromagnetic radiation, then adsorption can take place. As the frequency of the electric field of the infrared radiation approaches the frequency of the oscillating bond dipole and the two oscillate at the same frequency and phase, the chemical bond can absorb the infrared photon and increase its vibrational quantum number by +1, or what is the same, increase its vibrational state to a higher level.

As a first approximation, the larger the strength of the bond the higher the frequency of the fundamental vibration. In the same way, the higher the masses of the atoms attached to the bond the lower the wavenumber of the fundamental vibration. As a general guide, the greater the number of groups of a particular type and more polar the bond, the more intense the band.

The infrared spectrum can be divided into two regions, one called the functional group region and the other the fingerprint region. The functional group region is generally considered to range from 4000 to $1500cm^{-1}$ and all frequencies below $1500cm^{-1}$ are considered characteristic of the fingerprint region. The fingerprint region involves molecular vibrations, usually bending motions, that are characteristic of the entire molecule or large fragments of the molecule. Thus these are used for identificati on. The functional group region tends to include motions, generally stretching vibrations, which are more localised and characteristic of the typical functional groups, found in organic molecules. While these bands are not very useful in confirming identity, they do provide some very useful information about the nature of the components that

make up the molecule.

Basically an IR spectrometer is composed by the source, the monochromator and the receptor. The ideal IR source would be one that would give a continuous and high radiant energy output over the entire IR region. The two sources in most common use are the Nernst Glower (heated up to $2200K$) and the Globar (heated to about $1500K$). In general, in all IR sources the radiant energy, which depends upon the temperature of the source, is low in the far infrared, and to obtain sufficient energy the slit width of the source has to be opened considerably with a corresponding decrease in resolution. Between the source and the detector there must be some kind of device to analyse the radiation so that an intensity can be evaluated for each wavelength resolution element. There are two basic types, namely, monochromators, used in dispersive instruments, and interferometers used in Fourier transform instruments. In a monochromator, a prism or a diffraction grating is used, separating the components of polychromatic radiation. For spectroscopic work a prism must be transparent to the particular wavelength region of interest and the dispersion of the prism must be as large as possible. The function of a grating, like that of a prism, is to provide monochromatic radiation from radiation composed of many wavelengths. A diffraction grating consists of a number of equally spaced slits, which diffract light by interference. The theoretical resolving power of a grating may be expressed as mN, where m is the order of the spectrum and N is the number of grooves or rulings on the grating. There are basically two types of diffraction gratings, the transmission and the reflectance types.

The final part of the spectrometer is the detector. The IR detector is a device that measures the IR energy of the source that has passed through the spectrometer. Their basic function is to change radiation energy into electrical energy, which can be generated to process a spectrum.

In the case of FTIR spectroscopy the spectra are recorded in the time domain followed by computer transformation into the frequency domain, rather than directly in the frequency domain, as is done by dispersive IR spectrometers. However, in spite such procedure seems more complicated, they have been outlined above the advantages to be gained with FTIR. To record in the time domain, interference has to be used to modulate the IR signal at a detectable frequency. This is done by means of the well known Michelson interferometer, which is used to produce a new signal (interferogram) of a much lower frequency which contains the same information as the original IR signal. In the Michelson interferometer radiation leaves the source and is split. Half is reflected to a stationary mirror and then back to the splitter. This radiation has travelled a fixed distance. The other half of the radiation from the source passes through the splitter and is reflected back by a movable mirror.

Therefore, the path length of this beam is variable. The two reflected beams recombine at the splitter, and they interfere. If the movable mirror moves away from the beam splitter at a constant speed, radiation reaching the detector goes through a steady sequence of maxima and minima as the interference alternates between constructive and destructive phases. A simple sine wave interference pattern is produced. Each peak indicates mirror travel of one half the wavelength of the laser. The accuracy of this measurement system means that the IR frequency scale is accurate and precise. In the FTIR instrument, the sample is placed between the output of the interferometer and the detector. The sample absorbs radiation of particular wavelengths. Therefore, the interferogram contains the spectrum of the source minus the spectrum of the sample. An interferogram of a reference (sample cell and solvent) is needed to obtain the spectrum of the sample. After an interferogram has been collected, a computer performs a Fast Fourier Transform, which results in a frequency domain trace (i.e. intensity vs. wavenumber) that is what one needs and knows. The detector used in an FTIR instrument must respond quickly because intensity changes are rapid (the moving mirror moves quickly). So, pyroelectric detectors or liquid nitrogen cooled photon detectors must be used, while thermal detectors are too slow. To achieve a good signal to noise ratio, many interferograms are obtained and then averaged. This can be done in less time than it would take a dispersive instrument to record one scan.

3.5 Experimental

An iron silicide layer was produced by $195KeV$ Fe^+ ion implantation with a dose of 2x10^{17} Fe$^+$/cm^2 into a chemically cleaned p-type $Si(111)$ wafer with a high current implanter from the DANPHYSIK A/S. During the implantation the substrate was heated at $T_i = 500°C$. After implantation, the samples were annealed in a N_2 atmosphere at $850°C$ for $90min$. X-ray di ffraction (XRD) pole figure $(CuK_\alpha = 0.154nm)$ and cross-sectional transmission electron microscopy (XTEM) were employed to check the phase and orientation, the results indicated that the buried layers is grown epitaxially on $(111)Si$ substrate with the relation of (202) / or $(220)\beta - FeSi_2//(111)Si$. Experimental details and structural analysis will be published elsewhere [55].

The infrared (IR) transmittance spectra were taken at room temperature (RT) in the range of $200 - 500cm^{-1}$ by a Perkin-Elmer 1430 spectrometer. Raman spectra were measured at RT between 150 and 550 cm^{-1} by dispersive spectrometer combined with a focal microscope. Laser produced light at $532.14nm$ was used for excitation.

PL measurements at 12 K were performed using the $632.4nm$ line of an $He - Ne$ laser with an average excitation flux of $250mW/cm^2$ for exciting light source, and focused over a circular area of $\sim 0.3mm$ in radius. The laser beam was chopped through

an acousto-optic modulator at a frequency of $114Hz$. The luminescence signal was analyzed by a single grating monochromator and detected by a liquid nitrogen-cooled Ge detector for the infra-red ($1.2 - 1.6\mu m$ spectral region). Spectra were recorded with a lock-in amplifier using the chopping frequency as a reference.

3.6 Results and discussion

The space group of $\beta - FeSi_2$ is Cmca $\left(D_{2h}^{18}\right)$, N°64 [56]. The atomic structure of this orthorhombic phase has been described by Dusausoy et al. [34]. The $\beta - FeSi_2$ have a very complex unusual crystalline structure containing 48 atoms/unit cell. Fe atoms were surrounded by eight Si atoms with slightly different $Fe - Si$ distances, and we can note that the iron atoms occupy two different sites (Fe_I and Fe_{II}) and since this is also true for silicon (Si_I and Si_{II}) atoms.

The irreducible representations of each site were reported by Rousseau et al. [57], the B_{1u},B_{2u} and B_{3u} modes are infrared-active and A_{1g}, B_{1g}, B_{2g}, B_{3g} modes are Raman-active. The total of the expected modes is 72 including the 3 translations and 3 rotations of the whole crystal, and it agrees with the $3n$ modes (n=number of atoms in the primitive cell=24) predicted by group theory. For the D_{2h}^{18} structures, the u modes (ungerade) are IR-active and the g modes (gerade) are Raman-active while the A_u mode is a silent mode, not active in IR nor in Raman. Indeed, the dipolar momentum operator transforms itself like the transition vectors T_z, T_y and T_x , i.e respectively like , B_{1u}, B_{2u} and B_{3u} [58, 59].

The infrared (IR) transmittance spectra were taken at RT in the range of 200-500 cm^{-1} for different samples are shown in figure 3.3. We can assign the five main peaks to the five active IR internal modes of the iron sites characteristic for $\beta - FeSi_2$, their frequencies are 263.79, 300, 310, 344 and $425cm^{-1}$. These frequencies are in very good agreement with those previously published by Daraktchieva et al [4].

The IR spectra of the as-implanted samples and annealed samples at 850 °C for 90 min are compared, and they show the process on the formation of $\beta - FeSi_2$; the absorption at $310cm^{-1}$ can be explained by an initial nucleation of $\beta - FeSi_2$ precipitates during the implantation of iron into silicon substrate.

Figure 3.4 shows the Raman scattering spectrum obtained at RT from the sample annealed at 850°C for 90 min. The crystalline silicon has a typical line at 520 cm^{-1}. If the silicon becomes amorphous, this line disappears [60, 58]. The Raman signals are clearly identified at $173cm^{-1}$, $192.3cm^{-1}$, $198cm^{-1}$ and $245cm^{-1}$ which are found to originate from $Fe - Si$ vibrational modes [61], reflecting the formation of $\beta - FeSi_2$ phase. In comparison with the annealed sample, the Raman peaks of the as-implanted sample are located at 186.5, 240 and $507cm^{-1}$ (for the latter frequency

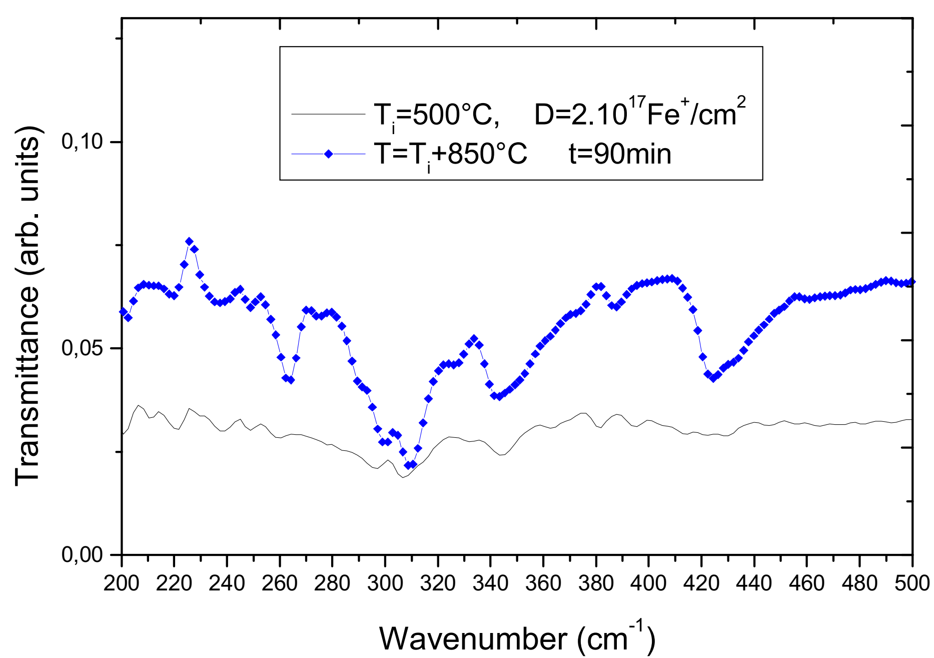

Figure 3.3: IR Spectra of samples before (as-implanted at $T_i = 500°C$) and annealing in N_2 atmosphere for $90min$ at $850°C$

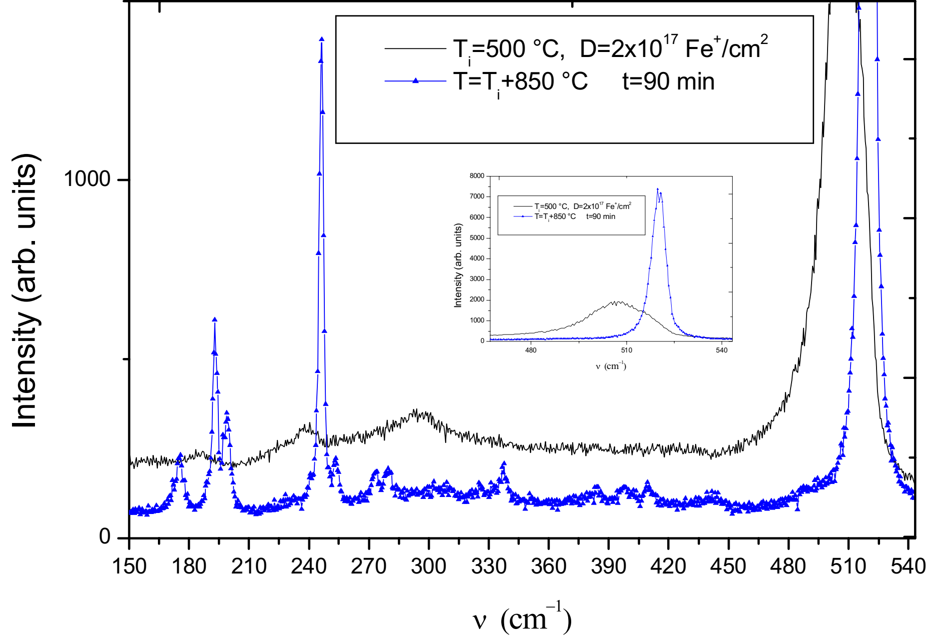

Figure 3.4: Raman scattering spectra at RT for the as-implanted and annealed samples.

see insert, figure 3.4), have smallest intensities and are red-shifted.

All experimental signals for $\beta - FeSi_2$ are slightly shifted toward lower energies compared to those obtained theoretically [60]. This shift may be explained by the stress caused during the implantation and the heat treatment.

PL spectrum at $12K$ for sample annealed at $850°C$ for $90min$ is shown in figure 3.5. The main feature is an intense peak at $0.811eV$ with a line width of approximately $17meV$ and we assign this peak to optical radiative transitions intrinsic to $\beta - FeSi_2$. This light emission, at the wavelength of $1.53\mu m$, corresponds to the band gap energy of $\beta - FeSi_2$. The peak, the position of which coincides with that of the well known $D1$ line emission ($0.807eV$) at high temperature due to the dislocations in silicon matrix [62], must be come from the $\beta - FeSi_2$ precipitates in our case of PL measurements performed at low temperature, as already reported [63].

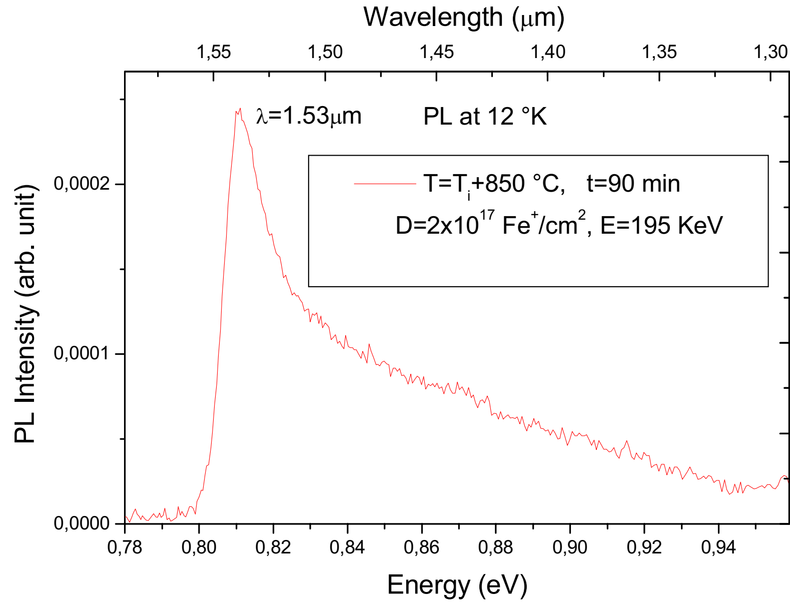

Figure 3.5: Photoluminescence spectrum of $\beta - FeSi_2$ precipitate layer at $T = 12\ K$ for the sample annealed in a N_2 atmosphere during $90min$ at $850°C$.

3.7 Conclusion

The $\beta - FeSi_2$ phase was fabricated by IBS with a dose of 2x10^{17} Fe^+/cm^2 in $(111)Si$ substrates at $500°C$ followed by annealing at $850°C$ for $90min$. The infrared transmittance spectra show the five mean peaks of $\beta - FeSi_2$. The Raman signals for $\beta - FeSi_2$ are slightly shifted toward lower energies. In PL measurements, the mean intense peak was observed at $0.811eV$ and we assign this PL peak to optical radiative transitions intrinsic to $\beta - FeSi_2$. No PL emission was observed for the as-implanted samples.

Chapter 4

Structural and optical properties of $\beta - FeSi_2$ phase prepared by IBS

Part I

Influence of implantation temperature

4.1 Experimental details

The $(111)Si$ p-type substrate was implanted with a $195KeV$ beam of ^{56}Fe at a current density of $11\mu A/cm^2$ and a dose of $2x10^{17}Fe^+/cm^2$, the tilt angle of the substrate relative to the beam was $7°$. The implantation was carried out at $440°C$. The as-implanted samples were then annealed in N_2 atmosphere at $900°C$ for $4h$.

Rutherford backscattering measurements were performed on the as-implanted and annealed samples, with $1.7MeV$ He^+ ions at a scattering angle of $170°$ between the incoming and outgoing beam line, and the experimental spectra were analyzed with Rump computer program [50]. XRD pole figure measurements were performed in a $\theta - 2\theta$ geometry using CuK_α radiation. Raman spectra were measured at room temperature (RT) between 150 and $600cm^{-1}$ by dispersive spectrometer combined with a focal microscope. Laser produced light at $532.15nm$ was used for excitation. PL measurements were performed at $12K$ using the $633.4nm$ line of the $He-Ne$ laser. The emission was detected using a liquid nitrogen-cooled Ge detector.

4.1.1 Results and discussion

Figure 4.1a shows the RBS spectrum of $(111)Si$ sample in the as-implanted state with an ion dose of $2x10^{17}Fe^+/cm^2$ at a substrate temperature of $440°C$, obtained in the random direction. The arrows (labeled Fe and Si) indicate the energy for backscattering from these elements at the surface. The Rump simulation of RBS spectrum allowed to obtain the depth profiles of Si and Fe elements (see figure 4.1b) and to confirm the formation of buried $FeSi_2$ layer during the ion implantation.

Figure 4.2 shows the RBS spectra of the as-implanted and annealed samples. As can be seen, the height of Fe signal decreases whereas the energetic width increases. In the same time the Si signal, around channel 500, corresponding to the buried layer is extended to the surface.

Figure 4.3a shows the XRD pole figures of the as-implanted sample. The poles are measured with steps of $5°$ of ϕ and χ angles (ϕ is the rotation angle around the surface normal and χ is the tilt angle of the sample) in the whole range of ϕ and in the range $\chi = 25-50°$. The poles with heights of $33.18, 42.70$ and 56.97 are produced by the tails of the $(111)Si$ reflections (Its maximum is located at $2\theta = 28.443°$) of the substrate. They give the orientation of the substrate. At the scattering angle $2\theta = 29.112°$, the poles with the heights of $5.57, 6.84$ and 6.88 which located at $85°/35°, 200°/40°$ and $315°/35°$ in the ϕ/χ coordinates respectively are $(220)\beta - FeSi_2/(202)\beta - FeSi_2$ reflections. This shows that the $\beta-FeSi_2$ crystals are oriented in the Si substrate. Furthermore, the intensity peak in the centre of the pole figure indicates $\beta-FeSi_2$ crystals with a fiber texture. Their epitaxial relationship is described as follows: $(220)\beta-FeSi2$

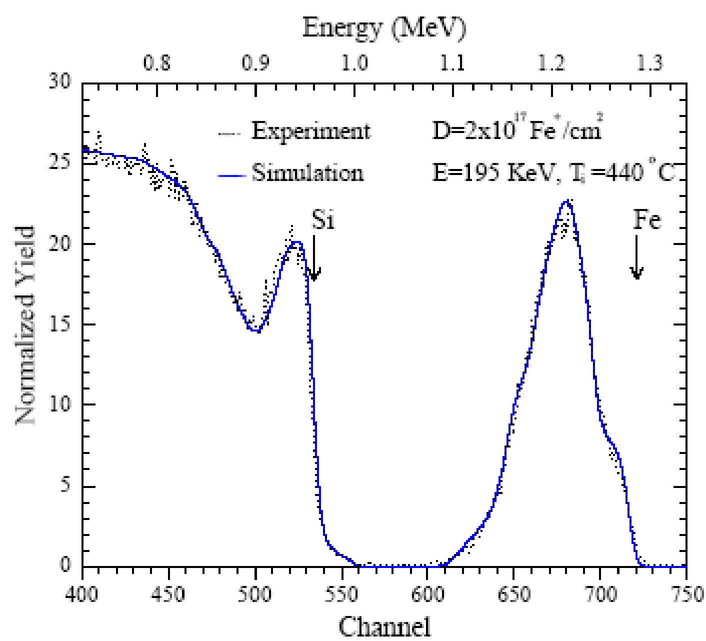

(a)

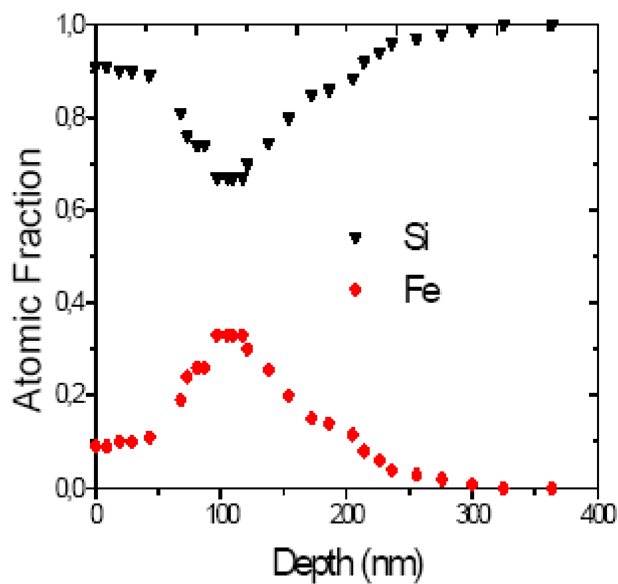

(b)

Figure 4.1: (*a*) RBS spectrum for the as-implanted samples, (*b*) Fe and Si depth profiles deduced from (*a*).

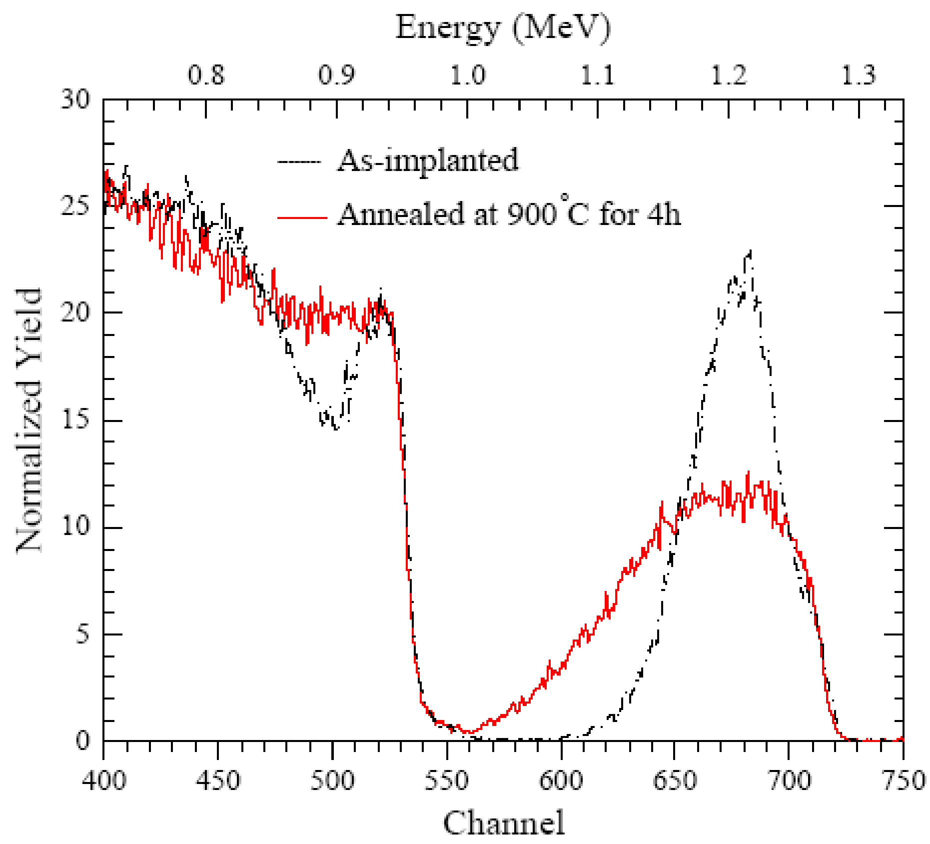

Figure 4.2: RBS spectra for the as-implanted and annealed samples.

and / or $(202)\beta - FeSi_2||(111)Si$. It should be noticed that only a very small amount of $\alpha - FeSi_2$ phase was found in this sample.

The XRD pole figures of the annealed sample in N_2 atmosphere at $900°C$ for $4h$ are shown in figure 4.3b. As can be seen, the three poles near the centre and at scattering angle $2\theta = 29.112°$ with the heights of $8.01, 15.02$ and 10.60 (with $\phi/\chi : 150°/30°, 260°/40°$ and $10°/30°$ respectively) are $(220)\beta - FeSi_2/(202)\beta - FeSi_2$ reflections. The other peaks are produced by the tails of $(111)Si$ reflections at $2\theta = 28.443°$.

These results indicate also the formation of epitaxial (220) and / or $(202)\beta - FeSi_2$ on the $(111)Si$ substrate.

The intensities of three poles of $\beta - FeSi_2$ are increased in the case of the annealed sample, attesting the increase in amount of $\beta - FeSi_2$ (width of a buried layer).

Figure 4.4 shows the Raman scattering spectra obtained at RT from the as-implanted and annealed samples. The crystalline silicon has a typical line at $520cm^{-1}$. If the silicon becomes amorphous, this line disappears [60, 58]. The Raman signals of the annealed sample are clearly identified at $175.8, 194.5, 198.2$ and $247.5cm^{-1}$, which are found to originate from $Fe - Si$ vibrational modes [61], reflecting the formation of $\beta - FeSi_2$ phase. The additional weak peak at $303.5cm^{-1}$ is originated from the silicon substrate (the LA phonon). In comparison with the annealed sample, the Raman peaks of the as-implanted sample are located at $186.7, 241.2$ and $515.2cm^{-1}$, have smallest intensities and are red-shifted. All experimental signals for $\beta - FeSi_2$ are slightly shifted toward lower energies compared to those obtained theoretically [61]. This shift may be explained by the stress caused during the implantation and the heat treatment.

PL spectrum obtained at $12K$ for sample annealed at $T_a = 900°C$ for $4h$ is shown in figure 4.5. The main feature is an intense peak at $0.81eV$ with a line width of approximately $29meV$ and we assign this peak to optical radiative transitions intrinsic to $\beta - FeSi_2$. This light emission, at the wavelength of $1.53\mu m$, corresponds to the band gap energy of $\beta - FeSi_2$. The peak of PL measurements performed at low temperature must be come from the $\beta - FeSi_2$ precipitates, as already reported [63]. It is important to notice that the peak position coincides with that of the well known $D1$ line emission ($0.807eV$) recorded at high temperature [62].

4.1.2 Conclusion

The $\beta - FeSi_2$ phase was fabricated by IBS with a dose of $2x10^{17}Fe^+/cm^2$ in $(111)Si$ substrates at $440°C$ followed by annealing at $900°C$ for $4h$. The buried layer is grown epitaxially on $(111)Si$ substrate with the relation of (220) and/or $(202)\beta -$

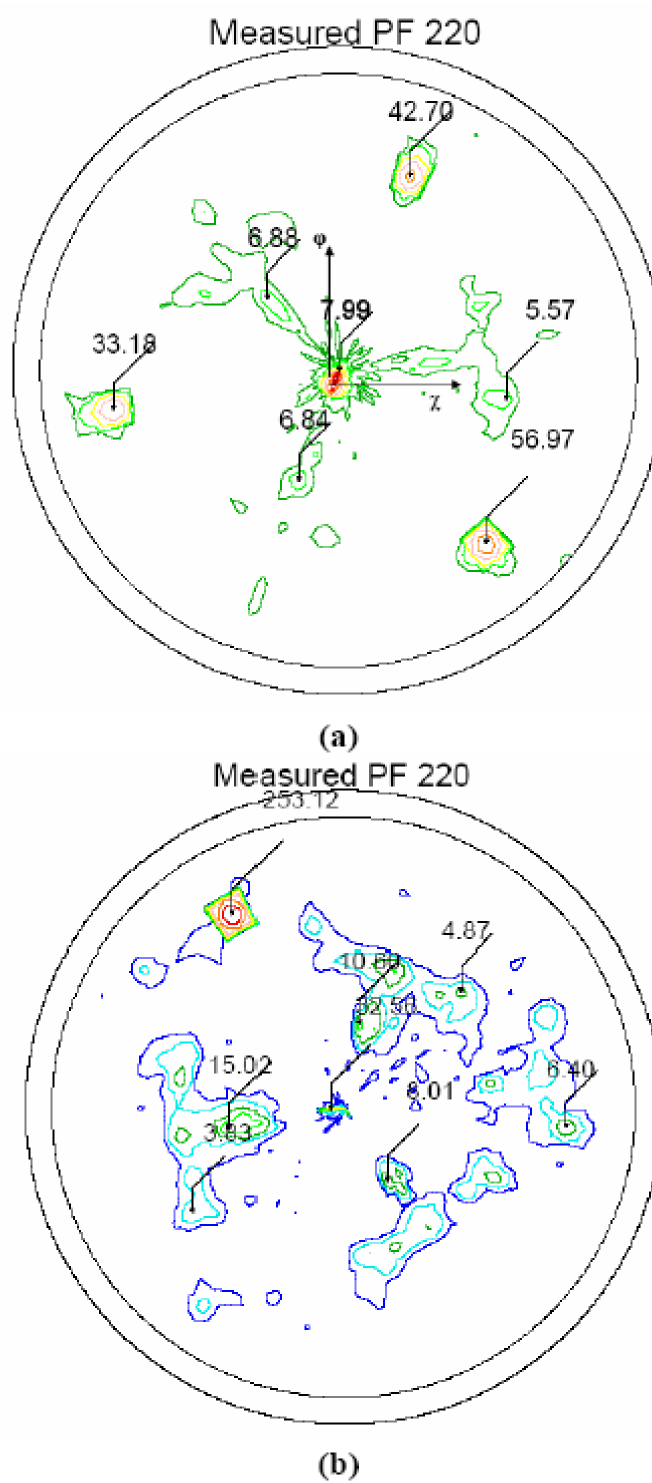

Figure 4.3: XRD pole figures for the as-implanted (a) and annealed (b) samples.

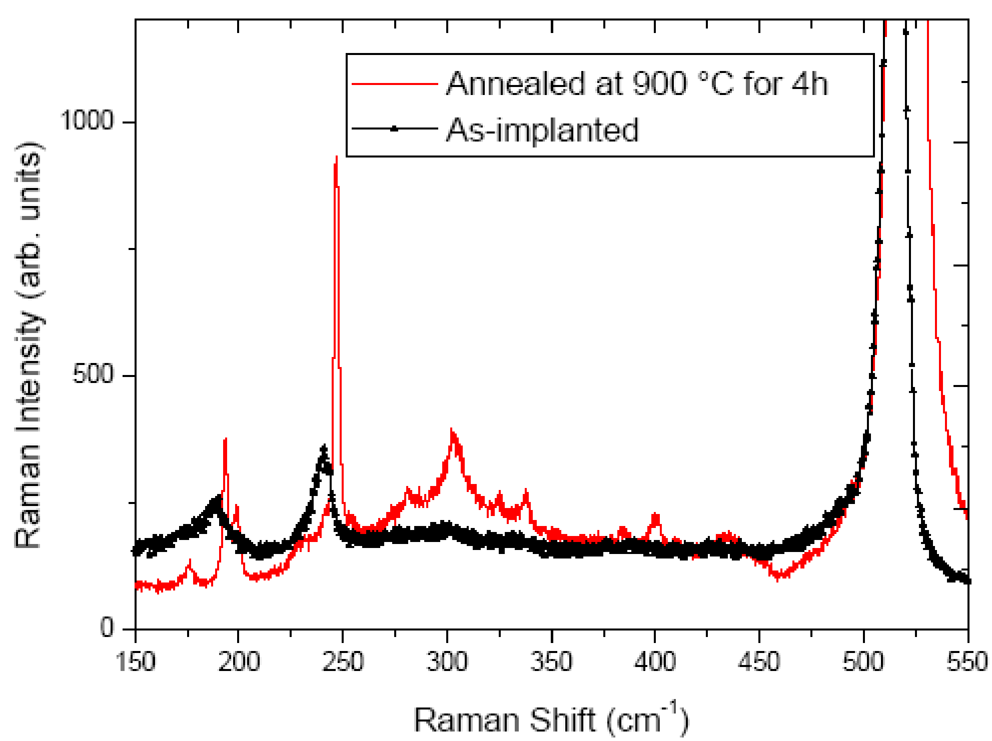

Figure 4.4: Raman scattering spectra at RT for the as-implanted and annealed samples.

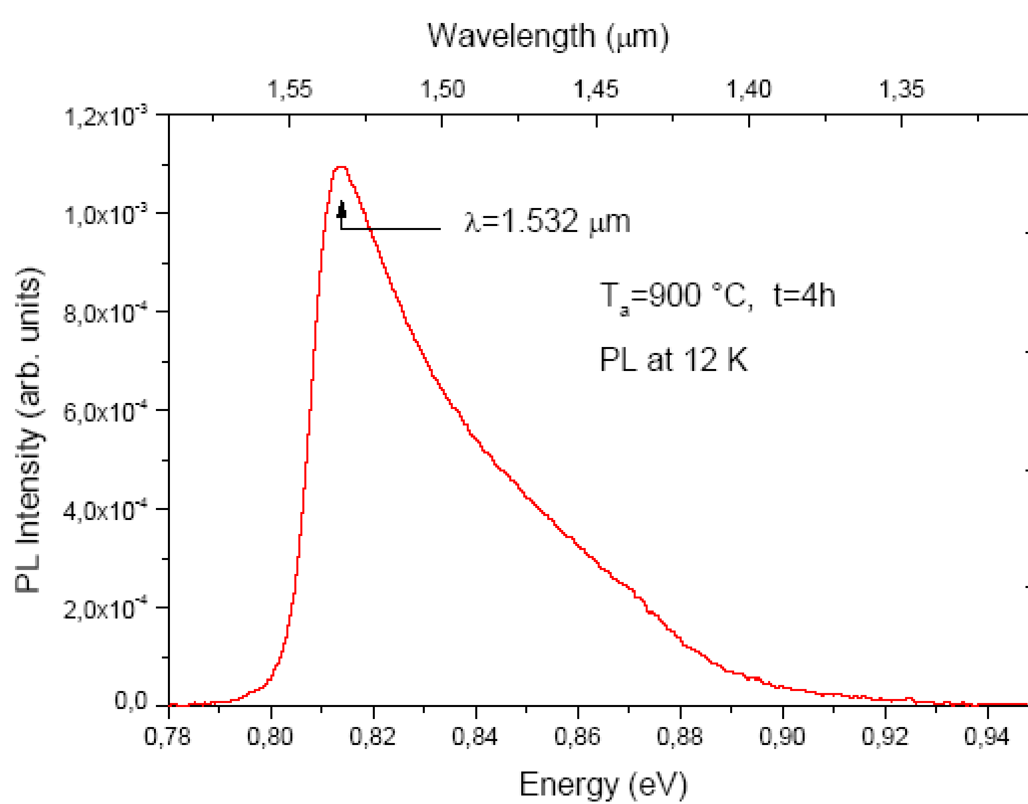

Figure 4.5: PL spectrum measured at $12K$ of $\beta - FeSi_2$ layer for the annealed sample.

$FeSi_2||(111)Si$. The Raman signals for $\beta - FeSi_2$ are slightly shifted toward lower energies. In PL measurements, the intense peak was observed at $0.81eV$ which is assigned to optical radiative transitions intrinsic to $\beta - FeSi_2$ silicide. No PL emission was observed for the as-implanted samples.

Part II

Influence of dose

4.2 Experimental procedure

The semiconducting iron disilicide ($\beta - FeSi_2$) samples were fabricated by implanting at room temperature with a dose of $8x10^{17} Fe^+/cm^2$ and an energy of $195keV$ into a p-type single crystal $Si(111)$ wafer. The ion source is a DANFYSIK high current implanter operated at 20-200 keV with magnetic scan, current limit < 10 mA, and target station with possibilities to move large of heavy samples. The sample was tilted by $7°$ to achieve a random implantation. After the implantation, all the samples were annealed in nitrogen atmosphere at $850°C$ for different times. Rutherford backscattering measurements were performed on the as-implanted and annealed samples, with $1.7MeV\ He^+$ ions at a scattering angle of $170°$ between the incoming and outgoing beam line, using a Si-surface barrier detector with resolution of $15keV\ FWHM$, and the experimental spectra were analyzed with Rump computer program [50]. The phase structure was monitored via $1°$ grazing-angle X-ray diffraction (XRD) with rotation of samples using CuK_α radiation. Cross-sectional transmission electron microscopy (XTEM) analysis was applied for phase identification and structural characterization. The infrared (IR) transmittance spectra were taken at room temperature (RT) in the range of $150 - 550cm^{-1}$ by an Equinox55/Bruker spectrometer. Raman spectra were measured at room temperature (RT) between 150 and $550cm^{-1}$ by dispersive spectrometer combined with a focal microscope.

4.2.1 Results and discussion

Figure 4.6a shows the RBS spectrum of a $(111)Si$ sample in the as-implanted state at room temperature with an ion dose of $8x10^{17} Fe^+/cm^2$, obtained in the random direction. The arrows (labeled Fe and Si) indicate the energy for backscattering from these elements at the surface. The Rump simulation of RBS spectrum allowed to obtain the depth profiles of Si and Fe elements (see figure 4.6b) and to confirm the formation of a $Fe - Si$ intermixed layer during the ion implantation.

Figure 4.7 shows the RBS spectra of the as-implanted and annealed samples at $850°C$ for different times. As it can be seen, the height of Fe signal decreases whereas the energetic width increases. In the same time the Si signal corresponding to the layer is extended. Also oxygen and carbon were found in the annealed samples.

XRD profiles from the as-implanted and annealed samples are shown in figure 4.8. An annealing at $850°C$ for different time , X-ray diffraction measurements show diffraction peaks of the $\beta - FeSi_2$ phase and of $Fe - C$ and $Fe - O$ compounds. So it can be concluded that ion implantation of such a high fluence at RT produces an

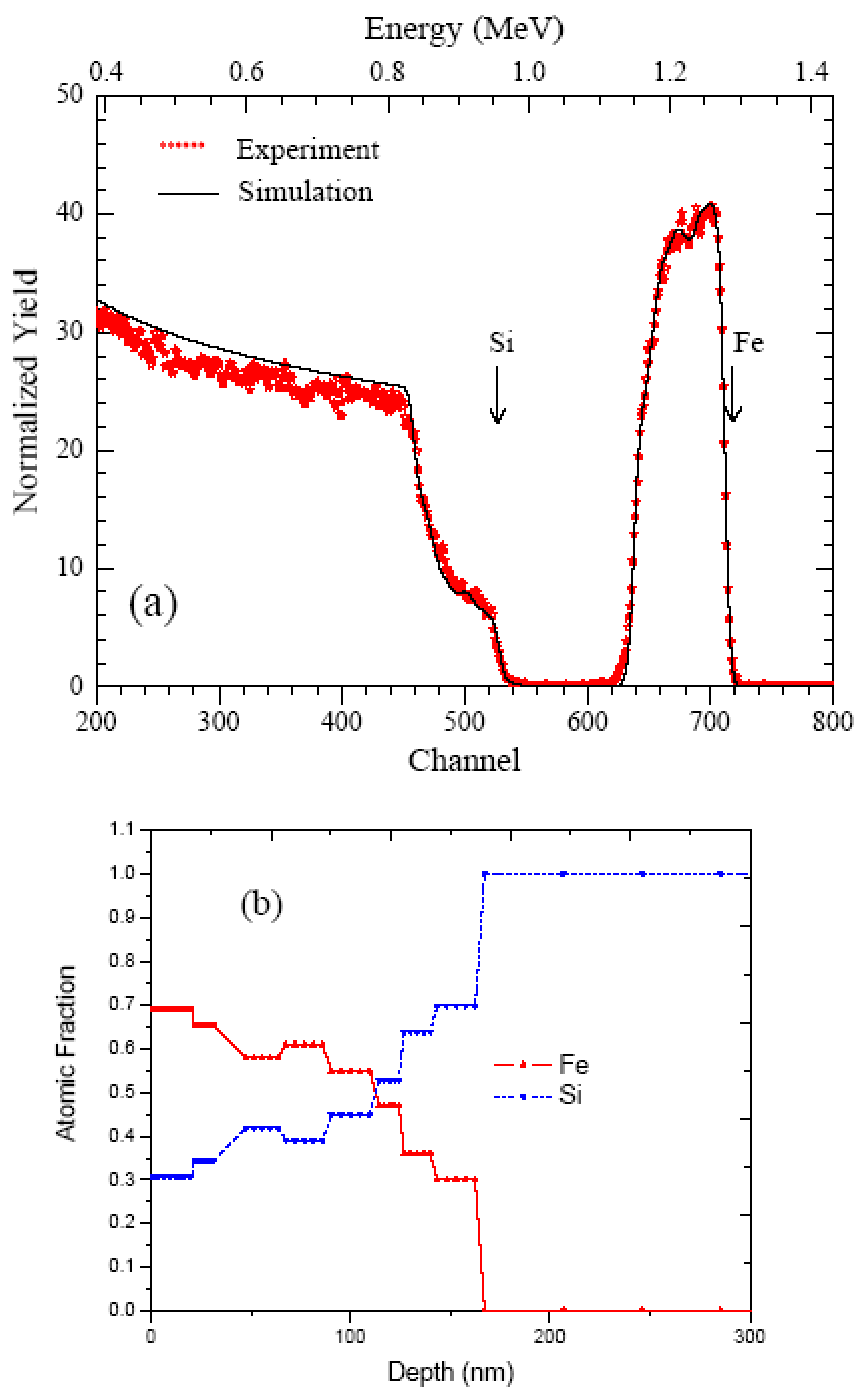

Figure 4.6: (a) Random RBS data for the as-implanted samples at RT. (b) Fe and Si depth profile deduced from the RUMP analysis.

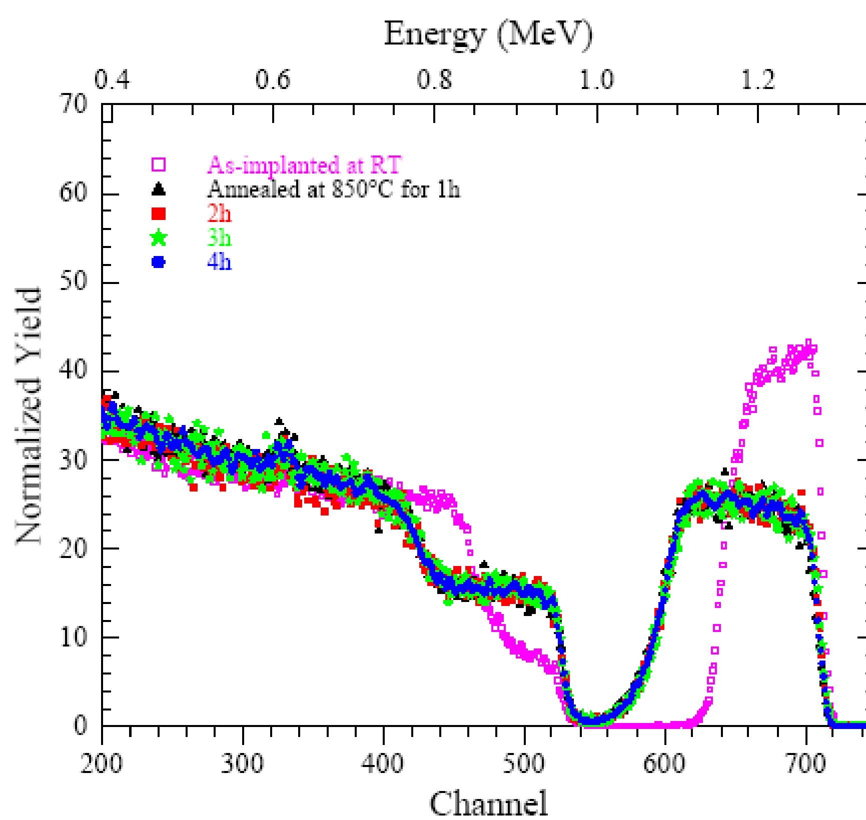

Figure 4.7: RBS spectra for the as-implanted and annealed samples at $850°C$ for different times.

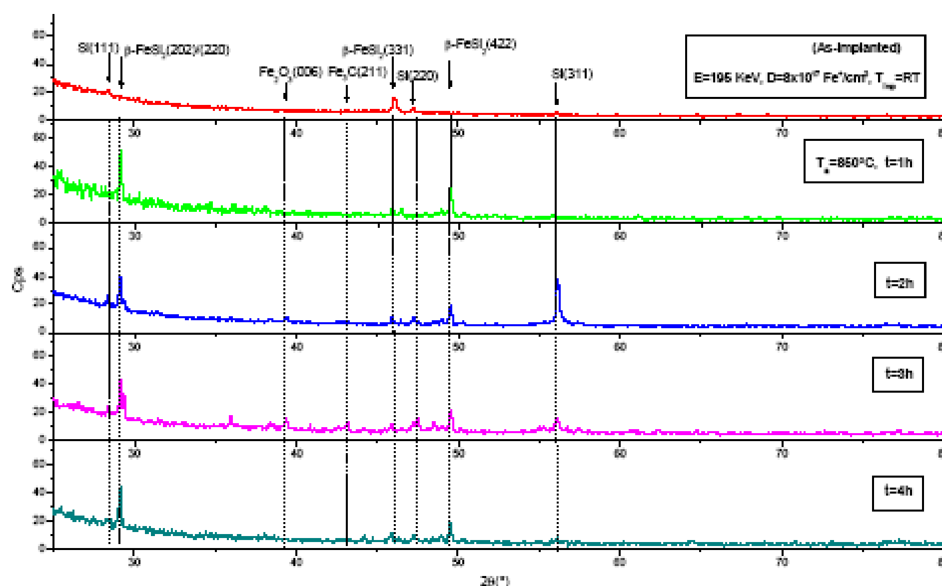

Figure 4.8: XRD patterns of the as-implanted and annealed samples for different annealing time at 850°C.

amorphous layer of Si mixed with the implanted Fe atoms. This layer does not recrystallize epitaxially but rather in polycrystalline form with a more or less orientation of the crystals; and $\beta - FeSi_2$ phase is polycrystalline with a crystallographic orientation determined by the random orientation of Si crystals, this was verified by XRD pole figures measurements (not shown), and no any indication of a preferred orientation of the $\beta - FeSi_2$ crystallites maybe seen.

Figure 4.9 shows cross-sectional TEM images of the as-implanted and annealed samples at 850°C for $4h$. The viewing direction is [110] of Si. The structure consists of three layers in the as-implanted sample (figure 4.9a): a top layer of amorphous-iron disilicide, a layer of ion implantation damage in the middle, and the crystalline silicon substrate at the bottom. While the layer itself is relatively smooth the border between amorphous Si (directly close to the interface) and crystalline Si is very rough. The diffraction pattern (inset figure 4.9a) clearly indicates the existence of $\beta - FeSi_2$. In the annealed sample (figure 4.9b), the layer is thicker and very rough (corresponding to interface to Si). Most of the grains run from the interface to surface. The examination of the continuous layer confirms that, after this heat treatment, the nature of the layer is not modified. However, the $\beta - FeSi_2$ layer becomes more homogeneous and flat with a thickness of about $0.2\mu m$.

The infrared (IR) transmittance spectra taken at RT in the range of $150 - 550cm^{-1}$

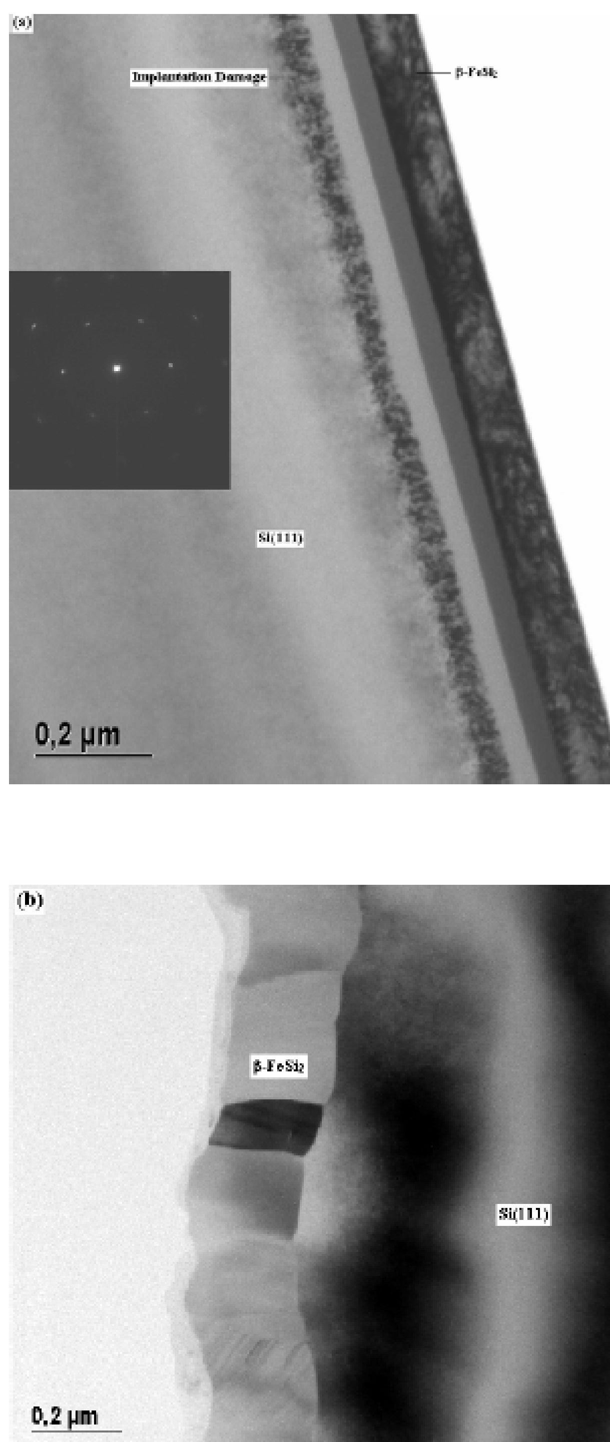

Figure 4.9: Cross-sectional TEM images of 195 keV Fe^{+} implanted $(111)Si$ substrate at RT with a dose of $8x10^{17}Fe^{+}/cm^{2}$: (a) as-implanted, (b) annealed in a N_2 atmosphere at $850°C$ for $4h$. The inset (Fig. 4.9a) shows the corresponding electron diffraction pattern of the $\beta - FeSi_2$.

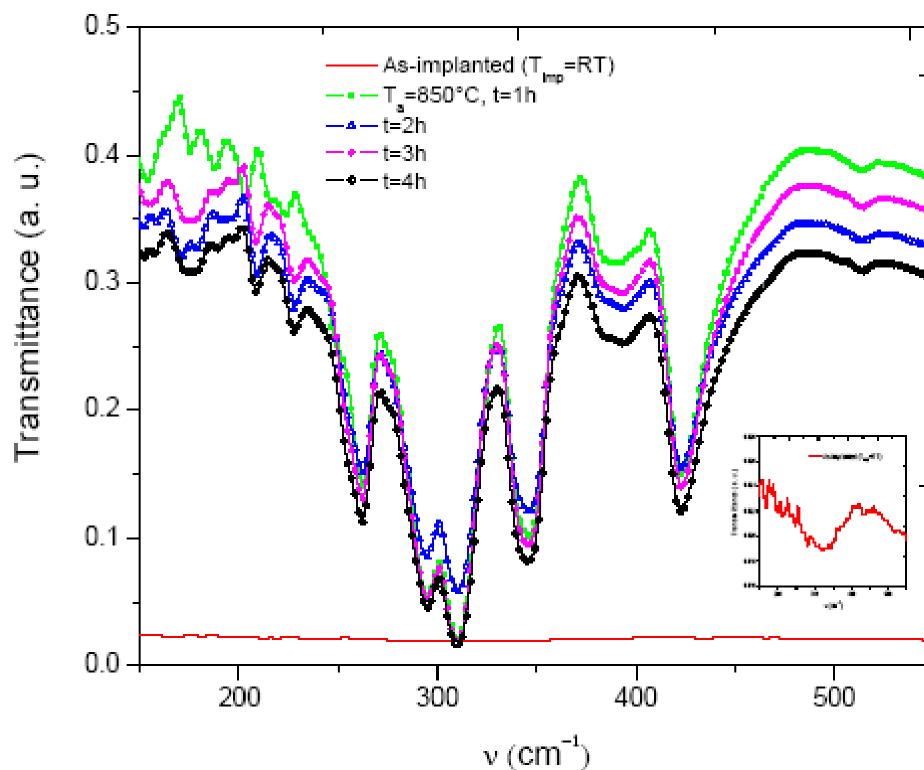

Figure 4.10: IR spectra for the as-implanted and annealed samples.Inset shows the latter transmittance for the as-implanted sample.

for as-implanted and annealed samples are shown in figure 4.10. The five main peaks can be assigned to the five active IR internal modes of the iron sites characteristic for $\beta - FeSi_2$, their frequencies are $262.4, 295.1, 310, 345.3$ and $422.2cm^{-1}$. These frequencies are in a good agreement with those previously published by Daraktchieva et al.[4].

The IR spectra of the as-implanted and annealed samples at $850°C$ for different time are comparable and they reveal the formation of $\beta - FeSi_2$ phase. The absorption at $310cm^{-1}$ can be explained by an initial nucleation of $\beta - FeSi_2$ precipitates during the implantation of iron into silicon substrate (for the latter transmittance see inset, figure 4.10). Figure 4.11 illustrates the Raman scattering spectra obtained at RT from the as-implanted and annealed samples for different annealing time at $850°C$. As it can be seen, no lines were detected in the as-implanted sample, because the amount of $\beta - FeSi_2$ is too small. In comparison with the annealed sample, the Raman peaks have different intensities, which are $Fe - Si$ vibrational modes [61], reflecting the formation of $\beta - FeSi_2$ phase. We notice that all experimental peaks are red shifted

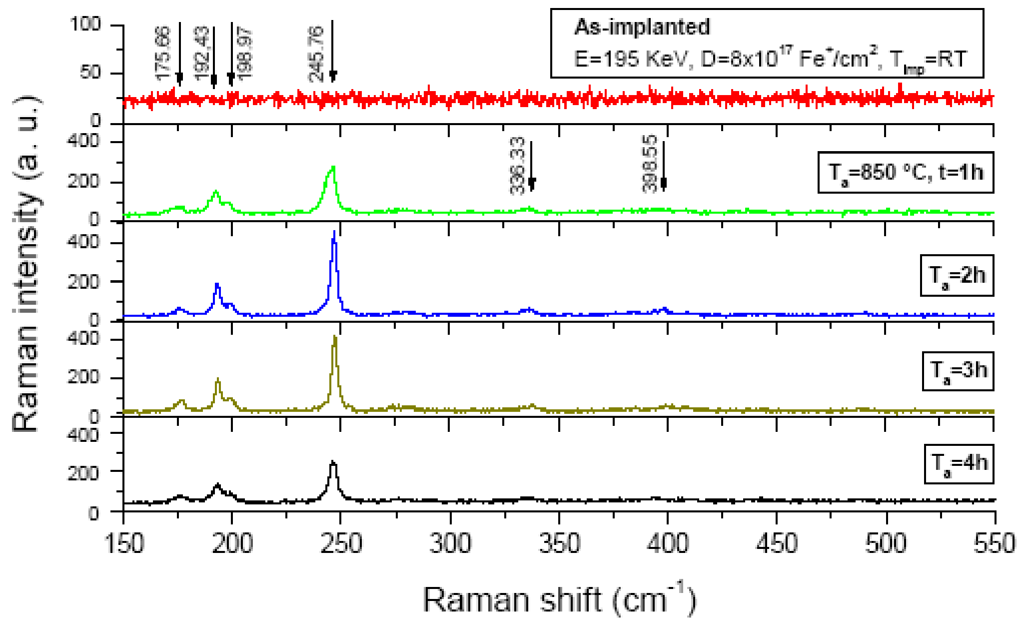

Figure 4.11: Raman scattering spectrum at RT for the as-implanted and annealed samples.

compared to those obtained theoretically [61]. This shift may be explained by the stress caused during the implantation and the heat treatment.

4.2.2 Conclusion

$\beta - FeSi_2$ phase was fabricated by IBS with a dose of $8x10^{17}Fe^{+}/cm^{2}$ in $(111)Si$ substrates at RT followed by an annealing at $850°C$ for different times. $\beta-FeSi_2$ phase is polycrystalline with a random crystallographic orientation. The IR transmittance spectra show the five main peaks of $\beta-FeSi_2$, and the absorption at $310cm^{-1}$ indicates the initial nucleation of $\beta - FeSi_2$ precipitates during the implantation. The Raman signals for $\beta - FeSi_2$ are slightly shifted toward lower energies.

Summary

A buried layer of iron disilicide was synthesized by ion implantation in *(1 1 1) S*i p-type maintained at *500 °C* using *195 keV Fe* ions with a dose of 2×10^{17} *at./cm*^{2}, followed by annealing in a N_2 atmosphere at 850 *°C* for *90 min*. The investigation of the phase composition is carried out by Rutherford backscattering spectrometry (RBS), whereas the structural characterization is obtained by means of both X-ray diffraction (XRD) pole figure and cross-sectional transmission electron microscopy (XTEM). The precipitates favor epitaxial growth with respect to *(1 1 1) Si* planes with epitaxial relationships *(2 2 0)* β-$FeSi_2$ || *(1 1 1) Si* and/or *(2 0 2)* β-$FeSi_2$ || *(1 1 1) Si*. A mixture of β-$FeSi_2$ and α-$FeSi_2$ silicides is observed in the as-implanted state. After annealing of the samples at 1000 *°C*, the XRD pole figures show the transition from β-phase to α-phase.
Semiconducting iron disilicide (β–$FeSi_2$) was prepared also by ion beam synthesis (IBS) in *(111)Si* P-type by implantation at *440 ˚C* of *195 KeV Fe* ions with a dose of $2x10^{17}$ Fe^{+}/cm^2 followed by annealing in a N_2 atmosphere at *900 ˚C* for *4 h.* The buried layer is grown epitaxially on *(111)Si* substrate with the relation of *(220)* and/or *(202)* β-$FeSi_2$ || *(111)Si.*
The processes in the synthesis of a thin layer of the semiconducting iron silicide (β-$FeSi_2$) on the surface of a single-crystal *(111)Si* substrate by implantation of *195 KeV Fe* ions with a dose of $8x10^{17}$ Fe^{+}/cm^2 are investigated and β-$FeSi_2$ phase is polycrystalline with a crystallographic orientation determined by the random orientation of *Si* crystals.
The Thin β-$FeSi_2$ layers in all cases have been characterized by means of infrared and Raman spectroscopies. The infrared (IR) transmittance spectra show the absorption at $310\ cm^{-1}$ as an indication of the initial nucleation of β-$FeSi_2$ precipitates during the implantation of iron into silicon substrate. The shift in Raman signals may be explained by the stress caused during the implantation and the heat treatment or due to crystalline defects of β-$FeSi_2$. The main feature of the photoluminescence (PL) measurements at *12 K* in the β-$FeSi_2$/*(1 1 1)Si* samples is an intense peak localized at *0.811 eV*. This peak is assigned to optical radiative transitions intrinsic to β-$FeSi_2$.

Bibliography

[1] J. E. Mahan, V. Le Thanh, J. Chevrier, I. Berbezier and J. Derrien, J. Appl. Phys. 74 (1993) 1747.

[2] M. Ozvold, V. Bohac, V. Gasparik, G. Leggieri, S. Luby, A. Luches, E. Majkova and P. Mrafko , Thin Solid Films 263 (1995) 92.

[3] H. Lange, Thin Solid Films 381(2001) 171.

[4] V. Daraktchieva, M. Beleva, E. Garonova and Ch. Angelov, Vacuum 58 (2000) 415.

[5] N. Kobayashi, H. Katsumata, H. L. Shen, M. Hasegawa, Y. Makita, H. Shibata, S. Kimura, A. Obara, S. Uekusa and T. Hatano, Thin Solid Films 270 (1995) 406.

[6] A. Heinrich, H. Griessmann, G. Behr, K. Ivanko, J. Schumannn and H. Vinzelberg, Thin Solid Films 381 (2001) 287.

[7] Y. Makita, in proceedings of the Japan-UK joint workshop on Kankyo-Semiconductors (Ecologically Friendly Semiconductors),edited by Y. Makita (Society of Kankyo Semiconductors in Japan, Japan, 1999 p. 1).

[8] I. Berbezier, J. L. Regolini and C. D'Anterroches, Microsc. Microanal. Microstruct. 4 (1993) 5.

[9] Y. Tsuyoshi, N. Tatsuya and N. Kunihito, Thin Solid Films 381 (2001) 236

[10] A. Terrasi, S. Ravesi, C. Spinella, M. G. Grimaldi and A. La Mantra, Thin solid Films 188 (1994) 241.

[11] N. P. Baradas, D. Panknin, E. Wiesser, B. Schmidt, M. Betzel, A. Mucklich and Skorupa, Nucl. Instr. and Meth. B 127-128 (1997) 316.

[12] M. Milosovljevic, S. Dhar, P. Schaaf, N. Blic, Y. L. Huang, M. Seibt and K. P. Lieb, J. Appl. Phys. 90 (2001) 4474.

[13] Y. V. Kudryavtsev, Y. P. Lee, J. Dubowik, Szymanski and J. Y. Rhee, Phys. Rev. B 65 (2002) 104417.

[14] D. Gerthsen, K. Radermacher, Ch. Deiker and S. Mantl, J. Appl. Phys. 71 (1992) 3788.

[15] D. J. Oostra, C. W. T. Bulle-Lieuwma, D. E. W. Vandenhoudt, F. Felten and J. C. Jans, J. Appl. Phys. 74 (1993) 4347.

[16] Z. Q. Liu, J. Y. Feng and W. Z. Li, Nucl. Instr. and Meth. B 197 (2002) 67.

[17] M.A. Nicolet, S.S. Lau, in: N.G. Einspruch, G.B. Larrabee (Eds.), VLSI Electronics Microstructure Science, Academic Press, New York, 1983.

[18] C. Calandra, 0. Bisi, G. Ottaviani, Surf. Sci. Rep. 4 (1981)271.

[19] W. MGnch, Rep. Prog. Phys. 53 (1990) 221.

[20] A. P. DE Jong and C. W. T. Bulle Lieuwma, Phi. Mag. A62,183 (1991)

[21] H. von Ka¨nel, K. A. Ma¨der, E. Mu¨ller, N. Onda, and H. Sirringhaus, Phys. Rev. B 45, 13807 (1992).

[22] W. J. Chen and F. R. Chen, Phi. Mag. A68, 605 (1993)

[23] M. Hansen, Constitution of Binary Alloys (McGraw–Hill, New. York,1958)

[24] C. Fu, M. Krijn, and S. Doniak, Phys. Rev. B 49, 2219 (1994).

[25] Villars and L. D. Calvert, Pearson's Handbook of Crystallographic Data for Intermetallic Phases (American Society for Metals, Material Park, OH, 1985).

[26] J. Alvarez, J. J. Hinarejos, E. G. Michel, and R. Miranda, Surf. Sci. 287, 490 (1993).

[27] U. Kafader, M. H. Tuilier, C. Pirri, P. Wetzel, G. Gewinner, D. Bolmont, O. Heckmann, D. Chandesris, and H. Magnan, Europhys. Lett. 22, 529 (1993).

[28] J. J. Hinarejos, G. R. Castro, P. Segovia, J. Alvarez, E. G. Michel, R. Miranda, A. Rodriguez-Marco, D. Sanchez-Portal, E. Artacho, F. Yndurain, S. H. Yang, P. Ordejon, and J. B. Adams, Phys. Rev. B 55, R16065 (1997).

[29] S. Walter, M. Kutschera, R. Bandorf, W. Weiss, M. Strass, M. Bockstedte, U. Starke, O. Pankratov, and K. Heinz, Phys. Rev. B (submitted).

[30] A. L. Vazques de Parga, J. de la Figuera, C. Ocal, and R. Miranda, Ultramicroscopy 42, 845 (1992).

[31] H. Sirringhaus, N. Onda, E. Mu¨ller-Gubler, P. Mu¨ller, R. Stalder, and H. von Ka¨nel, Phys. Rev. B 47, 10567 (1993).

[32] N. Jedrecy, A. Waldhauer, M. Sauvage-Simkin, R. Pinchaux, and Y. Zheng, Phys. Rev. B 49, 4725 (1994).

[33] J. Chevrier, P. Stocker, Le Thanh Vinh, J. M. Gay, and J. Derrien, Europhys. Lett. 22, 449 (1993).

[34] Y. Dusausoy, J. Protas, R. Wandji and B. Roques, Acta Crystallogr. B 27, 1209 (1971)

[35] N. Cherief, C. D'Anterroches, R. C. Cinti, T. A. Nguyen qnd J: Derrien; Appl. Phys. Lett. 55, 1971 (1989).

[36] S. Lagomarsino, F. Scarinci, C. Giannini, P. Castrucci, G. Savelli, J. Derrien, J. Chevrier, V. Le Thanh and M. G. Grimaldi, J. Vac. Scien. Technol B9, 2433 (1993).

[37] L. C. Feldman and J. W. Mayer, Fundamentals of Surface and Thin Film Analysis, Elsevier Science Publishing Co., Inc., New York, 1986.

[38] G. Dearnaley, J. H. Freeman, R. S. Nelson and J. Stephen, Ion Implantation, North-Holland Publishing Company, Amsterdam, 1973.

[39] J. W. Mayer, L. Eriksson and J. A. Davies, Ion Implantation into Semiconductors: Silicon and Germanium, Academic Press Inc., New York, 1970.

[40] S. P. Murarka, Silicides for VLSI Applications (Academic, Orlando, 1983).

[41] J. S. Williams and J. M Poate, Ion implantation and beam processing (Academic Press, 1984)

[42] A. R. Ramos, J. G. Marques, M. R. da Silva, O. Conde, M. F. da Silva and J. C. Soares, Nucl. Instr. Meth. B 161 (2000), 909.

[43] T. P. Sjoreen, H.-J. Hinnberg and M. F. Chisolm, Mater. Res. Soc. Symp. Proc. 279 (1993), 243.

[44] L. C. Feldman and J. W. Mayer, Fundamentals of Surface and Thin Film Analysis (Elsevier N. H.1986)

[45] W. K. Chu, J. W. Mayer and M. A. Nicolet, Backscattering Spectrometry (Academic Press 1978)

[46] Bond, W. L. . Acta Cryst. 13 (1960) 814–818.

[47] T. Garet, Transmission Electron Microscopy of Metals (John Wiley 1962)

[48] B. Fultz and J. M. Howe, Transmission Electron Microscopy and Diffractometry of Materials. Berlin Heidelberg New York: Springer-Verlag, 2001.

[49] Anita Peeva, Microstructural Characterization and Engineering of Defects in Silicon, FZR-387, 2003

[50] L. R. Doolittle, Nucl. Instr. and Meth. B 9 (1985) 344.

[51] D. Panknin, E. Wieser, K. Wollschlager, R. Grotzschel and W. Skorupa, Vacuum 44 (1993) 171.

[52] Y. Imai, M. Mukaida and T. Tsunoda, Thin Solid Films 381 (2001) 176.

[53] N. B. Colthup, L. H. Daly and S. E. Wberley, Introduction to Infrared and Raman Spectroscopy (Academic Press 2003)

[54] M. J. Pelletier, Analytical Applications of Raman Spectroscopy (Black Well Science 1999)

[55] R. Ayache, E. Richter and A. Bouabellou, Nucl. Instr. and Meth. B 216 (2004) 137-142.

[56] N. F. M. Henry and K. Lonsdale, Eds., International tables for X-ray crystallography (Kynoch, Birmingham, England, 1967) Vol. 1.

[57] D. L. Rousseau, R. P. Bauman and S. P. S. Porto, J. Raman Spectrosc. 10 (1981) 253.

[58] K. Lefki, P. Muret, E. Bustrarret, N. Boutarek, R. Madar, J. Chevrier, J. Derrien and M. Brunel, Solid State Communications, 80 (1991) 791.

[59] H. Kakemoto, Y. Makita, S. Sakuragi and T. Tsukamoto, Thin Solid Films, 381 (2001) 251.

[60] T. Yoshitake, T. Nagamoto and K. Nagayama, Thin Solid Films, 381 (2001) 236.

[61] H. Kakemoto, Y. Makita, S. Sakuragi and T. Tsukamoto, Jpn. J. Appl. Phys., 38 (1999) 5192.

[62] R. Sauer, J. Weber and J. Stolz, Appl. Phys. A,: Mater. Sci. Process., 36 (1985) 1.

[63] Y. Gao, S. P. Wong, W. Y. Cheung, G. Shao and K. P. Homewood, Appl. Phys. Lett., 83 (2003) 42.

[64] J. F. Ziegler, Ion implantation technology, Edgewater, 2000.

[65] J.P. Biersack, J.F. Ziegler, The Stopping and Range of Ions in Solids, Pergamon, New York, 1985.

الخواص البنيوية و الضوئية لسليسورات الحديد المحضرة بواسطة الغرس الأيوني

ملخص:

الشريحة الموا راة لسليسور الحديد (β-$FeSi_2$) حضرت عن طريق الحزمة الأيونية المصطنعة (الغرس الأيوني) في مساند من السليكون ذات الاتجاه (111) من النوع P، بواسطة غرس ايونات الحديد ذات طاقة 195 KeV و بجرعة $2x10^{17}$ Fe^{+}/cm^{2}، متبوعة بتحمية حرارية مابين 850 و1000°C تحت ضغط غاز النيتروجين.

التقنيات المستعملة لدراسة بنية الطور هي:

- مطيافية التشتت الخلفي لرذرفورد (RBS)
- إنعراج الأشعة السينية (XRD)
- المجهر الالكتروني النافذ (TEM)

نتائج هذه التحليلات وضحت بأن نمو حبيبات الطور كانت موازية للمستويات البلورية بالعلاقة التالية:

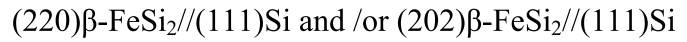

$(220)\beta\text{-}FeSi_2//(111)Si$ and /or $(202)\beta\text{-}FeSi_2//(111)Si$

لدراسة الخواص الضوئية لشرائح الطور(β-$FeSi_2$) تم تحليلها بواسطة مطيافية الأشعة تحت الحمراء (IR) و رامان (Raman) و كانت النتائج كالأتي: أطياف الأشعة تحت الحمراء النافذة بينت الامتصاص عند 310 cm^{-1} و هي مؤشر بداية نمو الطور خلال غرس أيونات الحديد داخل مساند السليكون. مطيافية رامان وضحت تزحزح خطوط الطيف نحو الأقل طاقة.

التحليل بواسطة الإضاءة الفوتونية (PL) لدى الدرجة 12 كالفن بين انبعاث خط الضوء بطاقة 0.811 eV، و هذا يعود إلى الإشعاع الضوئي الناتج عن الانتقال الذاتي داخل الطور β-$FeSi_2$.

Structural and optical properties of iron silicides synthesized by ion implantation

Abstract

A buried layer of iron disilicide (β–$FeSi_2$) is prepared by ion beam synthesis (IBS) in (1 1 1) Si P-type by implantation of 195 KeV Fe ions with a dose of $2x10^{17}$ Fe^+/cm^2 followed by annealing in nitrogen atmosphere between 850 and 1000˚C for different times. The investigation of the phase composition is carried out by Rutherford backscattering spectrometry (RBS), whereas the structural characterization is obtained by means of both X-ray diffraction (XRD) pole figure and cross-sectional transmission electron microscopy (XTEM). The precipitates favor epitaxial growth with respect to (1 1 1) Si planes with epitaxial relationships (2 2 0) β-$FeSi_2$ || (1 1 1) Si and/or (2 0 2) β-$FeSi_2$ || (1 1 1) Si.

For optical properties, the thin β-$FeSi_2$ layers have been characterized by means of infrared and Raman spectroscopies. The infrared (IR) transmittance spectra show the absorption at 310 cm^{-1} as an indication of the initial nucleation of β-$FeSi_2$ precipitates during the implantation of iron into silicon substrate. The Raman signals for β-$FeSi_2$ are slightly shifted toward lower energies. The main feature of the photoluminescence (PL) measurements at 12 K in the β-$FeSi_2$/(1 1 1)Si samples is an intense peak localized at 0.811 eV. This peak is assigned to optical radiative transitions intrinsic to β-$FeSi_2$.

Keywords: *Ion beam synthesis; β–$FeSi_2$; RBS; XRD pole figure; TEM; IR; Raman spectroscopy; PL.*

Propriétés structurales et optiques de siliciures de fer synthétisés par implantation ionique

Résumé:

Une couche enterrée du disiliciure de fer semiconducteur β-$FeSi_2$ est préparée à l'aide de faisceau d'ions (IBS) dans un substrat (111)Si de type P. La couche est obtenue par implantations d'ions de fer, avec une dose de $2x10^{17}$ Fe^+/cm^2 et une énergie égale à 195 KeV, suivie d'un recuit thermique effectué sous atmosphère de gaz inerte entre 850 et 1000°C pendant différents temps de maintien. L'analyse quantitative de la phase formée est réalisée à l'aide de la spectroscopie d'ions rétrodiffusés de Rutherford (RBS). La diffraction des rayons X en figures de pôle (XRD) et la microscopie électronique à transmission en coupes transversales (XTEM) sont utilisées pour les caractérisation structurales et microstructurales.

L'étude montre que la croissance des précipités β-$FeSi_2$ sur le substrat (111)Si est épitaxiale suivant la relation épitaxiale (220) β-$FeSi_2$ //(111)Si et/ou (202) β-$FeSi_2$ //(111)Si.

Les spectroscopies infra-rouge (IR) et Raman sont mises en œuvre pour la caractérisation optique des échantillons. Les spectres IR en transmission montrent une absorption à 310 cm^{-1}, ce qui atteste de la nucléation initiale de précipités β-$FeSi_2$ durant l'implantation Fe^+ dans (111)Si. Les raies Raman relatives au composé β-$FeSi_2$ sont légèrement décalées du côté des faibles énergies. La caractérisation principale des mesures de photoluminescence (PL), effectuées à 12 K, dans la structure β-$FeSi_2$ /(111)Si est l'apparition d'un pic intense localisé à 0,811 eV. Ce pic est assigné aux transitions optiques radiatives intrinsèques à la phase semiconductrice β-$FeSi_2$.

Mots clés: *IBS; β-$FeSi_2$; RBS; XRD en Figures pole; TEM en coupes transversales; Spectroscopies IR et Raman; Photoluminescence (PL).*